HOKKAIDO UNIVERSITY

Title	A three-dimensional constitutive model for rocks based on a variable elastic modulus
Author(s)	LI, Zhaoxin
Citation	北海道大学. 博士(工学) 甲第15384号
Issue Date	2023-03-23
DOI	10.14943/doctoral.k15384
Doc URL	http://hdl.handle.net/2115/89699
Type	theses (doctoral)
File Information	LI_Zhaoxin.pdf

Instructions for use

Hokkaido University Collection of Scholarly and Academic Papers : HUSCAP

A three-dimensional constitutive model for rocks based on a variable elastic modulus

Dissertation for the Degree of Doctor of Engineering

LI Zhaoxin

Laboratory of Global Resources and Environmental Systems

Division of Sustainable Resources Engineering

Graduate School of Engineering

Hokkaido University

March 2023

Acknowledgments

When I finished typing the last word for the doctor's dissertation, I sat up, pulled the curtains, opened the windows, and the noisy world turned into silence in the night, which made me re-think one important question after twenty-four years of studying on the road, do I keep a young heart?

It took me three and a half years to graduate from Japan with a Ph.D. Three and a half years ago, I went to Japan with the idea of reading and traveling a lot. Three and a half years later, I got my doctor's degree and saw a lot.

Reading a lot. I got my doctor's degree. There are many people I need to thank. Without their help, I could not have completed my thesis. First and foremost, I express my sincere gratitude to my supervisor, Professor Dr. Yoshiaki FUJII, for his valuable guidance, expert advice, encouragement, and constant support that led to the completion of my studies. His immense knowledge and great experience have always encouraged me in my academic research and daily life. I could not have imagined having a better advisor and mentor for my Ph.D. studies. Second, I also want to thank the Assoc. Prof. Dr. Jun-Ichi Kodama and Assoc. Prof. Dr. Diasuke Fukuda for their technical support on my study. Third, I would like to thank all the members of the Laboratory of Global Resources and Environmental Systems and the Rock Mechanics Laboratory. Their kind help and support have made my study and life in Japan wonderful. Fourth, I would like to express my thanks to all the professors of the Division of Sustainable Resources Engineering, Graduate School of Engineering, Hokkaido University, for their kind support. Fifth, I am grateful to the Ministry of Education, Culture, Sports and Science and Technology, Japan, for the doctoral scholarship (MEXT), the China Scholarship Council (CSC), and the English Engineering Education Program (e^3) for their support. Finally, I would like to express my gratitude to my family. Without their tremendous understanding and encouragement over the past few years, it would be impossible for me to complete my studies.

Traveling a lot is as important as reading a lot. I went to many places and met many people in my spare time. The purpose of traveling is to enjoy the scenery in other places and to re-examine my country by watching the scenery in other places. I got it. Thank you to all the people I meet.

In the end, I hope to keep a young heart, reading and traveling after years of fighting.

LI Zhaoxin

Engineering A654

Hokkaido University

Sapporo

Hokkaido

March 2023

Abstract

No constitutive equations can fully represent true triaxial stress-strain curves considering the effects of intermediate principal stress (σ_2), and a realistic curvilinear stress-strain relationship is needed for precise analyses of rock structures. Therefore, this study aims to propose a 3D constitutive model with fewer parameters, realistic stress-strain curves, and convex failure envelopes. Our research group previously proposed a simple two-dimensional (2D) constitutive model for rocks to simulate the axial stress–axial strain relationship and axial stress–lateral strain relationship, with few complicated equations. However, the failure envelope it predicted was linear and did not consider the effect of σ_2. This simple 2D model is modified in the present study to have a convex failure criterion. Then, the model is extended to a simple three-dimensional (3D) model that approximates true triaxial stress-strain curves for real rocks under specific values of σ_2 and minimum principal stress (σ_3) and uses only four parameters. However, the predicted peak stress–σ_2 relationship is linear. Finally, a modified 3D model is developed, which exhibits the true triaxial convex failure criterion. The equations in this model are simpler than the conventional true triaxial failure criterion, which cannot represent true triaxial stress-strain curves. A method to represent the axial unloading behavior is also proposed. The proposed models can be implemented with a finite element method (FEM) to improve the design of rock structures.

CONTENTS Page No.

1. Introduction

1.1 Background

The simplest three-dimensional (3D) constitutive model for rocks is

$$\sigma_1 = (\lambda + 2\mu)\varepsilon_1 + \lambda\varepsilon_2 + \lambda\varepsilon_3 \tag{1.1}$$

$$\sigma_2 = \lambda\varepsilon_1 + (\lambda + 2\mu)\varepsilon_2 + \lambda\varepsilon_3 \tag{1.2}$$

$$\sigma_3 = \lambda\varepsilon_1 + \lambda\varepsilon_2 + (\lambda + 2\mu)\varepsilon_3 \tag{1.3}$$

where ε_1, ε_2, and ε_3 are the maximum (axial), intermediate, and minimum (lateral) principal strains, respectively; σ_1, σ_2, and σ_3 are the maximum (axial), intermediate, and minimum (lateral) principal stresses, respectively; and λ and μ are Lame's constants (Fig. 1.1a and b).

Elasto-brittle models can be derived by introducing peak and residual strengths (Figs. 1.1 c, d, and e). However, the resulting stress-strain curves, which should be curvilinear for real rocks, are unrealistic polylines. More realistic stress–strain curves can be obtained using various two-dimensional (2D) constitutive models (Cristescu, 1987; Frantziskonis and Desai, 1987; Cristescu and Hunsch, 1991; Li et al., 1998; Okubo and Fukui, 2006; Weng, et al., 2008; Xie, et al., 2011; Zhang, et al., 2013; Pourhosseini and Shabanimashcool, 2014; Cecilio, et al. 2015; Wang, et al., 2018; Zhang, 2018; Ismael, et al., 2019).

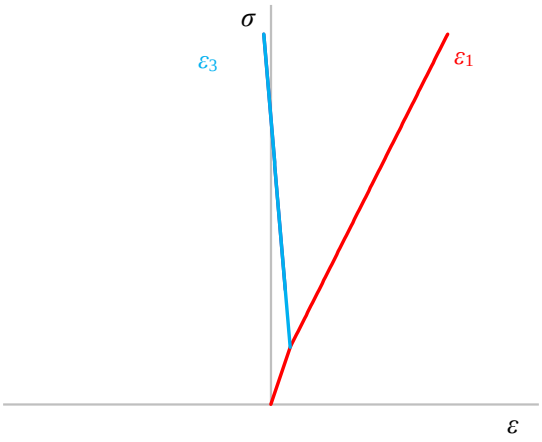

(a) $\sigma_2 = \sigma_3$

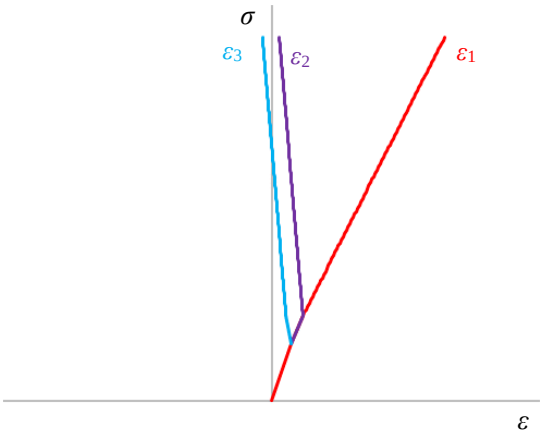

(b) $\sigma_2 > \sigma_3$

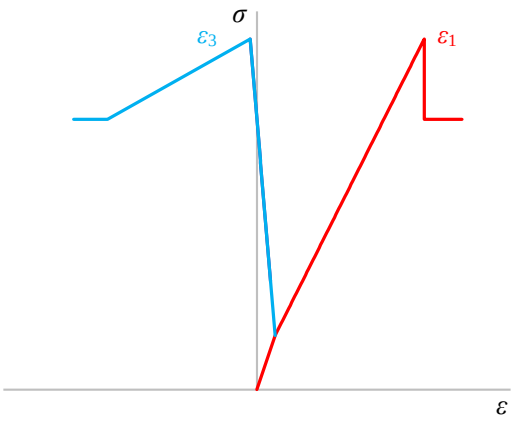

(c) $\sigma_2 = \sigma_3$

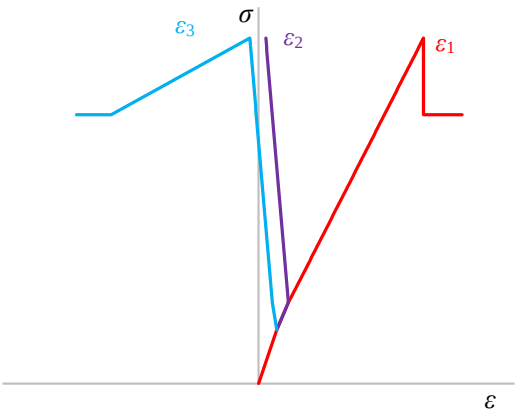

(d) $\sigma_2 > \sigma_3$

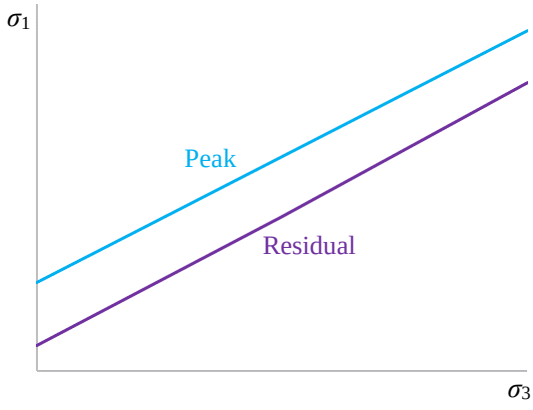

(e) failure criterion

Fig. 1.1 The simplest 3-D constitutive model under (a): uniaxial compression and (b): $\sigma_2 > \sigma_3$. A 3-D elasto-brittle model under (c): uniaxial compression and (d): $\sigma_2 > \sigma_3$. (e) failure criterion.

A variable-compliance-type constitutive model (Okubo and Fukui, 2006) is (Fig. 1.2)

$$\sigma_1 = (\omega / b)^{1/(n-3)} \varepsilon_1^{-m/(n-m)} \tag{1.4}$$

where $\omega = \mathrm{d}\psi/\mathrm{d}t$, $\psi = \varepsilon_1/\sigma_1$. n, m, and b are constants. This equation simulates the axial stress–axial strain relationships for classes I and II. However, no reasonable methods to evaluate the lateral strain have yet been provided. Actual rocks under compression show lateral dilatancy around peak stress in most cases due to the growth of axial microcracks (Hallbauer et al., 1973; Martin and Chandler, 1993; Lajtai, 1998; Cho et al., 2007); this growth is essential to the deformation and failure of rocks (Wawersik and Fairhurst, 1970). Therefore, the axial stress–lateral strain relationship is more important than the axial stress–axial strain relationship (Fujii et al., 1998; Singh and Singh, 2008).

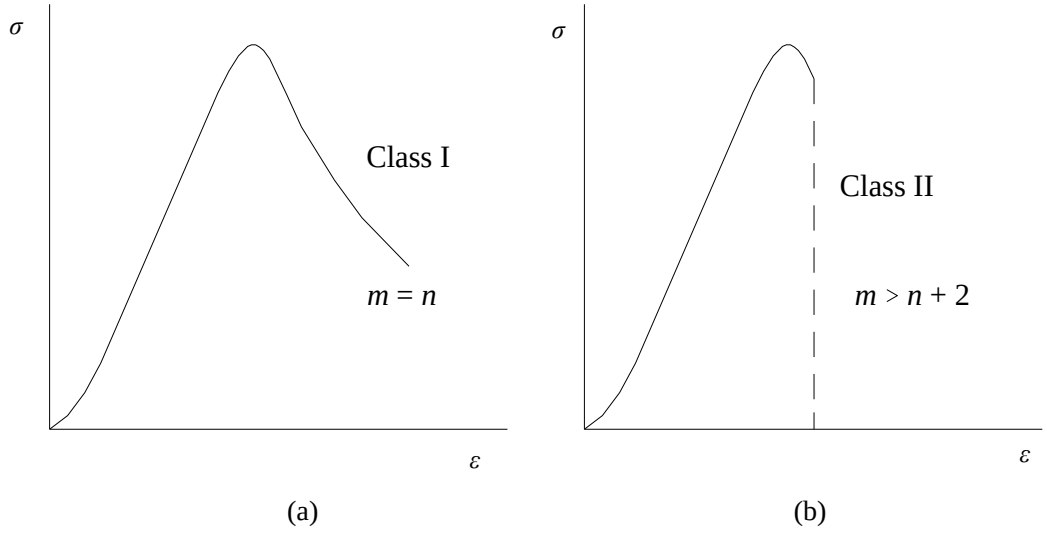

Fig. 1.2 A variable-compliance-type constitutive model (Okubo and Fukui, 2006).

By contrast, a simple 2D constitutive model for rocks was proposed by our research group (Fujii and Ishijima, 1998a) based on the finding that the trace of the axial strain, lateral strain, and axial stress is located on a plane in a 3D coordinate system for rocks such as Paleogene Kamisunagawa sandstone (Fig. 1.3, Fujii and Ishijima, 1998a), Cretaceous Pombetsu sandstone, Paleogene Bibai sandstone, and Paleogene Inada granite (Fujii and Ishijima, 1998b). The equations in the model are very simple, and class I and II strain-softening behaviors can be obtained with appropriate lateral strain behavior by introducing the strain-dependent elastic modulus.

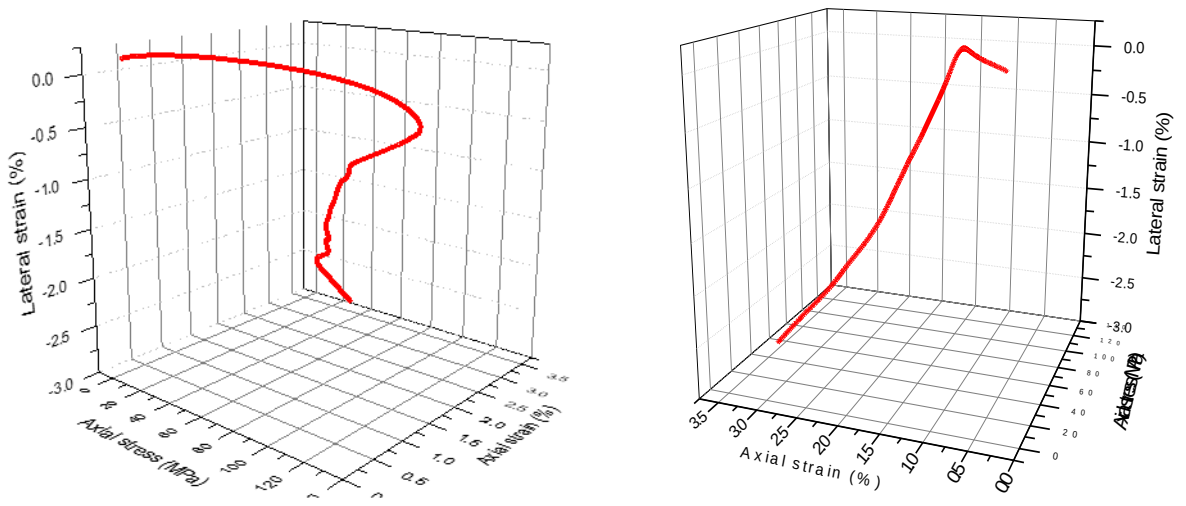

(a) (b)

Fig. 1.3 3D plots of strains and axial stress under uniaxial compression; after rotating the coordinate system, the originally curvilinear trace (a) appears as a straight-line (b) except for the initial loading stage.

For the 3D case, the strength of rocks is affected by σ_2 (Murrell, 1965; Mogi, 1967, 1971a, b, and 2007; Chang and Haimson, 2000; You, 2009; Senent et al., 2013; Fig. 1.4, Ma and Haimson, 2016; Feng et al., 2019), and various criteria have been proposed to describe these effects (Mogi, 1967, 1971a, b, and 2007; Lade and Duncan 1975; Pan and Hudson, 1988; Al-Ajmi and Zimmerman 2005; Priest, 2005; Zhang, 2007, 2008; Melkoumian et al., 2009; Jiang et al., 2011; Jiang and Zhao, 2015; Li et al., 2021). These criteria use complicated equations and many parameters. For example, a modified Lade criterion proposed by Ewy (1999) (Fig. 1.5) is represented as

$$(I_1')^3 / I_3' = 27 + \eta \tag{1.5}$$

$$I_1' = (\sigma_1 + s_1 - p_0) + (\sigma_2 + s_1 - p_0) + (\sigma_3 + s_1 - p_0) \tag{1.6}$$

$$I_3' = (\sigma_1 + s_1 - p_0) + (\sigma_2 + s_1 - p_0) + (\sigma_3 + s_1 - p_0) \tag{1.7}$$

where p_0 is pore pressure, η is related to the internal friction, and s_1 represents the cohesion of the rock. The peak strength increases and decreases with σ_2 according to the modified Lade criterion.

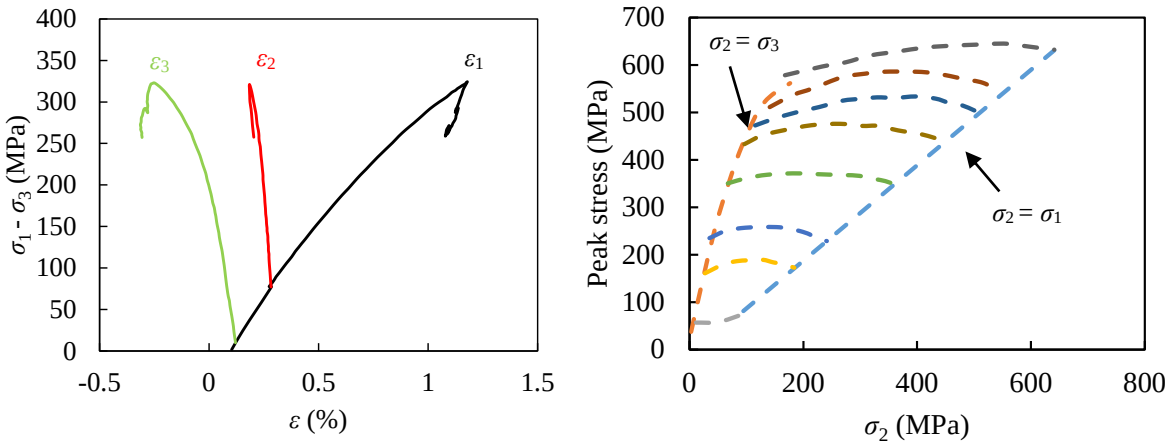

(a) Stress-strain curves (b) Failure envelopes

Fig. 1.4 True triaxial test results of Coconino sandstone (Ma and Haimson, 2016).

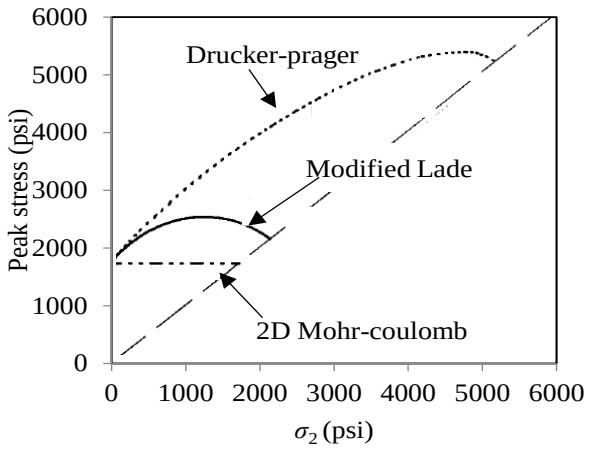

Fig. 1.5 Modified Lade criterion by s_0=500 Psi, φ = 30°, and σ_3 = 0 (Ewy, 1999).

As another example, a 3D failure criterion for rocks proposed by Li et al. (2021) based on the Hoek–Brown criterion (Hoek and Brown, 1980 and Hoek et al., 2002) is expressed as

$$\sigma_1 = \frac{b\sigma_2 + \sigma_3}{b+1} + \sigma_c \left(\frac{m_b}{\sigma_c} \frac{b\sigma_2 + \sigma_3}{b+1} + s \right)^{\alpha} \text{ (low } \sigma_2\text{)} \tag{1.8}$$

$$\frac{b\sigma_2 + \sigma_1}{b+1} = \sigma_3 + \sigma_c \left(\frac{m_b}{\sigma_c} \sigma_3 + s \right)^{\alpha} \text{ (high } \sigma_2\text{)} \tag{1.9}$$

where σ_c and b are the unconfined compressive strength and a constant, respectively, and

$$m_b = \exp\left(\frac{GSI - 100}{28 - 14D} \right) m_i \tag{1.10}$$

$$s = \exp\left(\frac{GSI - 100}{9 - 3D}\right) \tag{1.11}$$

$$\alpha = \frac{1}{2} + \frac{1}{6}\left(e^{-GSI/15} - e^{-20/3}\right) \tag{1.12}$$

where m_i, GSI, and D are the material constant for intact rock, geological strength index, and disturbance factor, respectively. The effects of σ_2 on rock strength are represented well in this model (Fig. 1.6); however, the parameter selection is complex, and the resulting peak stress curves are unrealistic polylines.

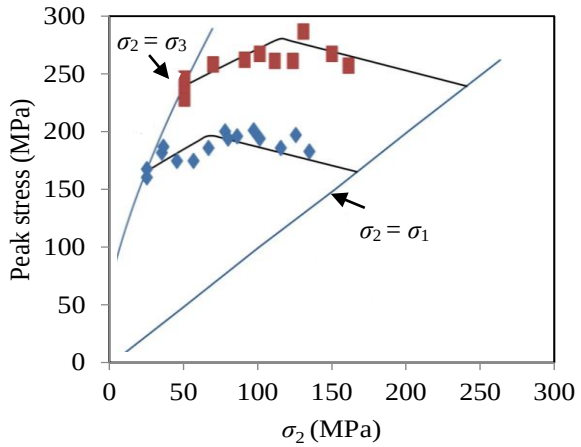

Fig. 1.6 3D HB criterion for Yuubari shale (Li, et al., 2021).

1.2 Objectives

No constitutive equations can fully represent true triaxial stress–strain curves considering the effects of σ_2. Therefore, the objective of this study is to propose a 3D constitutive model which can represent realistic true triaxial stress-strain curves and convex failure envelopes with fewer parameters.

1.3 Contents

The simple 2D constitutive model by Fujii and Ishijima (1998a) is briefly explained in chapter 1.4. Then, this simple model is modified to obtain the convex failure envelope by introducing stress dependency for an elastic modulus. An example of its application to a pressurized thick-walled cylinder under the plane strain condition in chapter 2 is given. Then, the simple 2D model is extended to a simple 3D one in chapter 3. Finally, this 3D model is modified to represent true triaxial stress–strain curves and convex failure

envelopes in chapter 4.

1.4 Simple 2D model

The simple 2D model developed by our research group should be briefly explained before the 3D models because they were developed based on the 2D model. A plane in the axial stress–axial strain–lateral strain space (Fig. 1.3) can be represented as

$$\sigma_1 = A(\varepsilon_1 - \varepsilon_0) + kA\varepsilon_3 \tag{1.13}$$

where A is an elastic modulus, and ε_0 and k are constants; these are equal to $\lambda+2\mu$, 0, and $\nu/(1-\nu)$, respectively, where ν is Poisson's ratio for a linear elastic medium.

Using a function of normal strain, $A'(\varepsilon)$, to replace the constant A, ignoring the constant ε_0 in Eq. 1.13 for simplicity,

$$\sigma_1 = A'(\varepsilon_1)\varepsilon_1 + kA\varepsilon_3 \tag{1.14}$$

By analogy, the following equation can be written for σ_3:

$$\sigma_3 = A'(\varepsilon_3)\varepsilon_3 + kA\varepsilon_1 \tag{1.15}$$

$A'(\varepsilon)$ should increase and converge to a specific value as ε tends to $+\infty$ (compression). The increase represents the increase in axial elastic modulus (A_A) due to microcrack closure (Fig. 1.7), as illustrated in Fig. 1.8a. $A'(\varepsilon)$ should also decrease with expansion and should converge to a specific value as ε tends to $-\infty$ (expansion). The decrease represents a decrease in the lateral elastic modulus (A_L) under extension due to the initiation and growth of axial microcracks (Fig. 1.7), as illustrated in Fig. 1.8b. These assumptions have already been confirmed numerically by a boundary element method combining displacement discontinuity (Crouch and Fairhurst, 1973) with the body force (Nishitani, 1994) elements in Fujii and Ishijima (1998b) and explained by various mechanisms (e.g., Fig. 1.9, Cho, et al., 2007; Zhao and Cai, 2010).

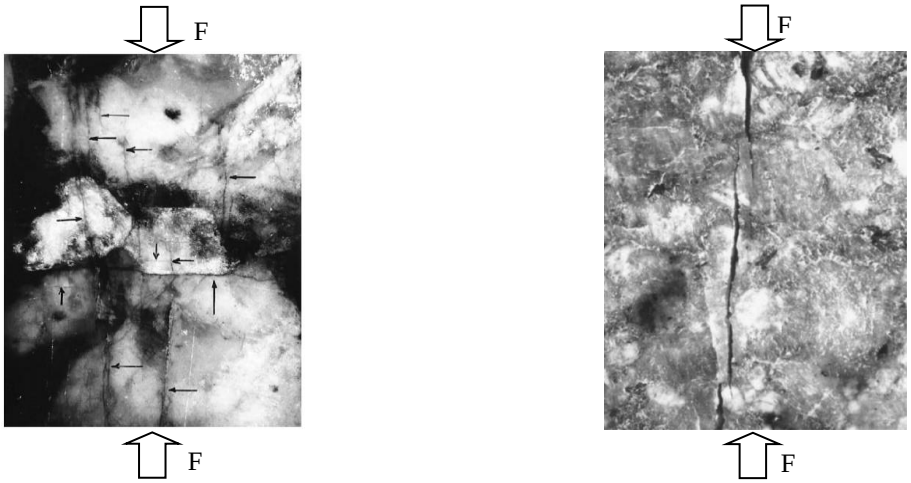

(a) (b)

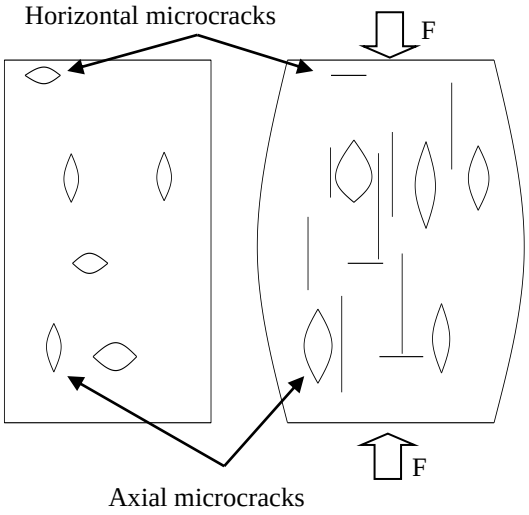

(c)

Fig. 1.7 (a): Cracks generated in the uniaxial compression test (vertical loading direction) in granite. The arrows are drawn perpendicular to the cracks. Most cracks are parallel to the loading direction (Lajtai, 1998). (b): Axial cracks generated in uniaxial compression test in granite (Cho et al., 2007). (c): Illustration of axial microcrack initiation and growth and horizontal microcrack closure.

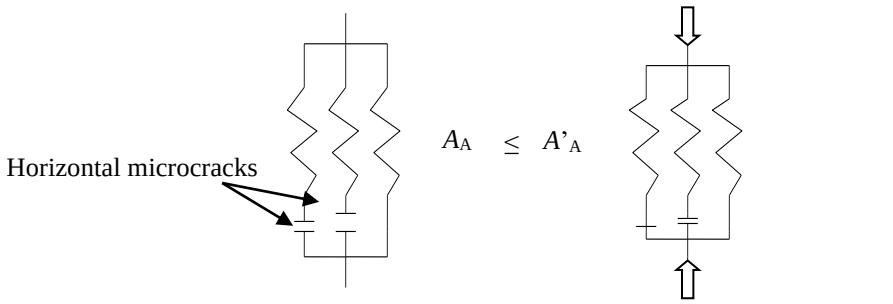

(a)

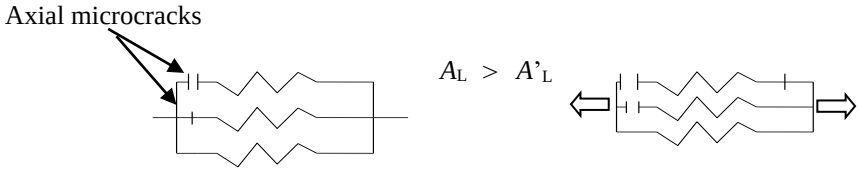

(b)

Fig. 1.8 (a): Increase in the axial elastic modulus due to compression. (b): Decrease in the lateral elastic modulus due to extension.

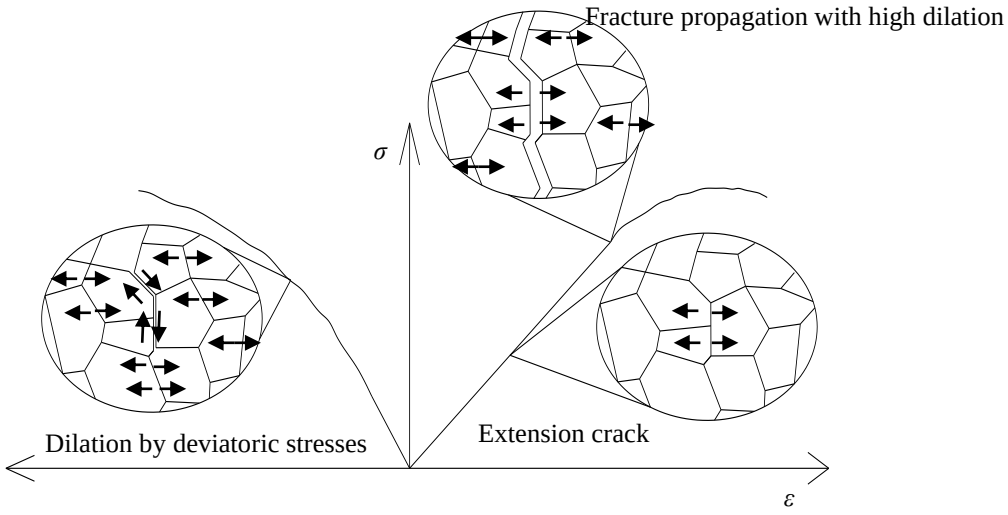

Fig. 1.9 Illustration of dilatation by axial microcrack initiation and growth in a laboratory test (Cho et al., 2007).

The following function (Fig. 1.10) was chosen as $A'(\varepsilon)$ to satisfy the above requirements:

$$A'(\varepsilon) = D\left[\tan^{-1}\left\{C\left(\frac{\varepsilon}{\varepsilon_s}+1\right)\right\}+\frac{\pi}{2}\right]+F \tag{1.16}$$

where ε_s is a constant whose value is approximately half the absolute value of the critical extensile strain (lateral strain value at the peak load point; Fujii et al., 1998), C is a positive constant, and D and F are determined so that the residual strength becomes constant as ε_1 and ε_3 tend to ∞ and $-\infty$, respectively as follows.

Assuming

$$A'(\varepsilon_1 = \infty) = A \tag{1.17}$$

As ε_3 tends to $-\infty$,

$$A'(\varepsilon_3 = -\infty) = F \tag{1.18}$$

Substituting Eqs. 1.17 and 1.18 into Eqs. 1.14 and 1.15,

$$\sigma_3(\varepsilon_1 = \infty, \varepsilon_3 = -\infty) = F\varepsilon_3 + kA\varepsilon_1 \tag{1.19}$$

$$\sigma_1(\varepsilon_1 = \infty, \varepsilon_3 = -\infty) = A\varepsilon_1 + kA\varepsilon_3 \tag{1.20}$$

Substituting Eq. 1.19 into Eq. 1.20,

$$\sigma_1(\varepsilon_1 = \infty, \varepsilon_3 = -\infty) = H'\varepsilon_1 + \frac{kA}{F}\sigma_3 \tag{1.21}$$

where,

$$H' = A - \frac{A^2k^2}{F} \tag{1.22}$$

Assuming $\sigma_1(\varepsilon_1 = \infty, \varepsilon_3 = -\infty) = \text{const.}$, H' should be 0,

$$\therefore \quad F = k^2A \tag{1.23}$$

$$D = \frac{(1-k^2)A}{\pi} \tag{1.24}$$

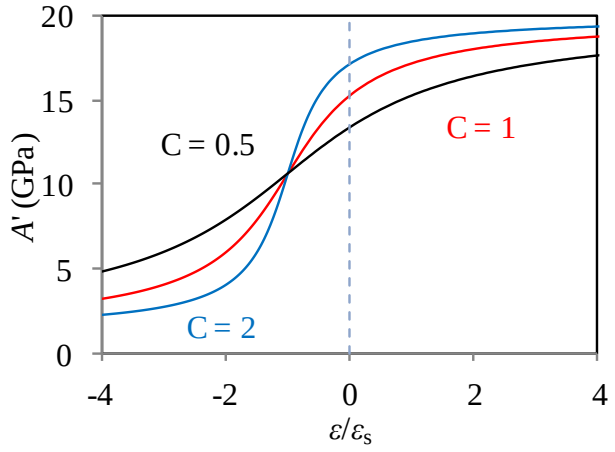

Fig. 1.10 Strain-dependent elastic modulus A' for A = 20 (GPa) and k = 0.25 (Fujii and Ishijima, 1998a).

From Eqs. 1.14−1.16, an ultimate residual strength, σ_{ur}, for infinite strains can be calculated as

$$\sigma_{ur} = \sigma_1(\varepsilon_1 = \infty, \varepsilon_3 = -\infty) = \frac{\sigma_3}{k} \tag{1.25}$$

However, the residual strength σ_r at −4.5% lateral strain (Fig. 1.11), which is higher than the ultimate residual strength, will be used hereafter for convenience.

The simple 2D model requires only four parameters (A, k, C, and ε_s) to simulate classes I and II nonlinear stress–strain behaviors (Figs. 1.11a−e), and tensile behavior can also be simulated seamlessly (Fig. 1.11a). Curves representing such behavior can be obtained as follows, for example:

(a1) Negative ε_3 increment (extensile) is assigned,

(a2) ε_1 is calculated by Eq. 1.15,

(a3) $A'(\varepsilon_1)$ and $A'(\varepsilon_3)$ are calculated by Eq. 1.16,

(a4) σ_1 can be calculated by Eq. 1.14,

(a5) Iterate steps (a2−a4) until the solution converges, and

(a6) Iterate steps (a1−a5) for loading until ε_3 reaches -0.045.

It is somewhat surprising that only a decrease in the lateral elastic modulus can induce strain-softening behavior. The mechanism of the strain-softening is as follows. The elastic modulus $A'(\varepsilon_3)$ decreases with lateral extensile strain, and this strain increases by Eq. 1.15. According to Eq. 1.14, the lateral extensile

strain increment causes a decrease in axial stress. The peak load point appears when the stress increase due to the axial strain increment becomes the same as the stress decrease due to the lateral extensile strain increment. In step (a1), the axial strain increment can be assigned instead of the lateral extensile strain one to simulate class I behavior.

Parameter A mainly affects the strength and tangent modulus (Fig. 1.11b). k mainly affects strength, the shape of the σ_1–ε_1 curve around the peak load, Poisson's ratio, and the critical compressive strain (ε_1 value at the peak load point; Fujii et al., 1998; Fig 1.11c). C mainly affects the shape of the stress–strain curves around the peak load, strength, and critical strains (Fig. 1.11d). ε_S mainly affects the critical strains and strength (Fig. 1.11e).

Because this model predicts a linear failure envelope (Fig. 1.12), it is modified in the next chapter. However, other results are similar to real rocks:

- Compressive strength increases with σ_3 (Fig. 1.11a),
- Compressive strength is larger than tensile strength (Fig. 1.11a),
- Critical compressive strain increases with σ_3 (Fig. 1.11f, Fujii, et al., 1998), and
- Critical extensile strain is unaffected by σ_3 (Fig. 1.11f, Fujii, et al., 1998).

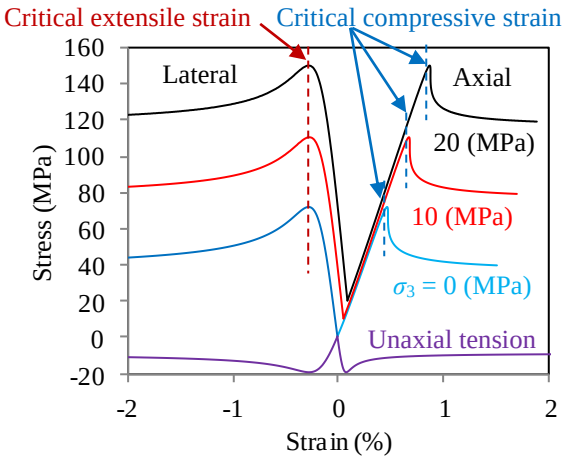

(a) Effects of σ_3

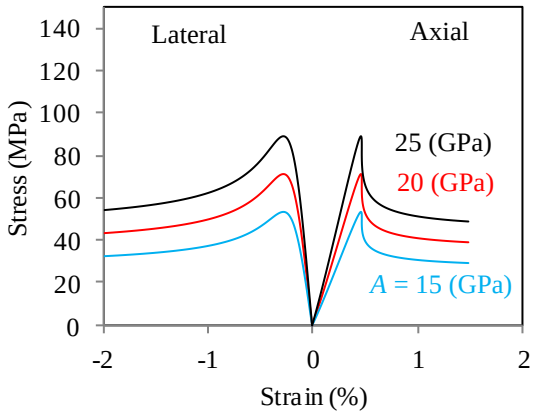

(b) Effects of A

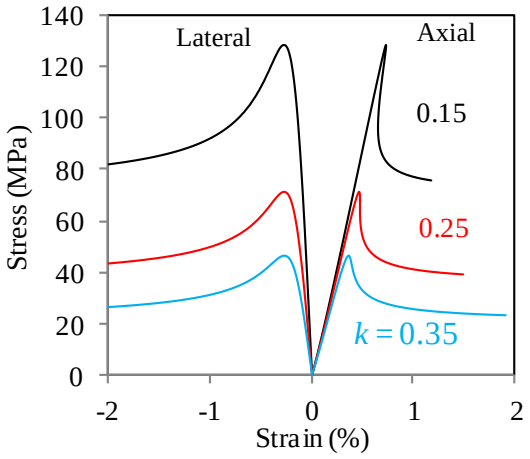

(c) Effects of k

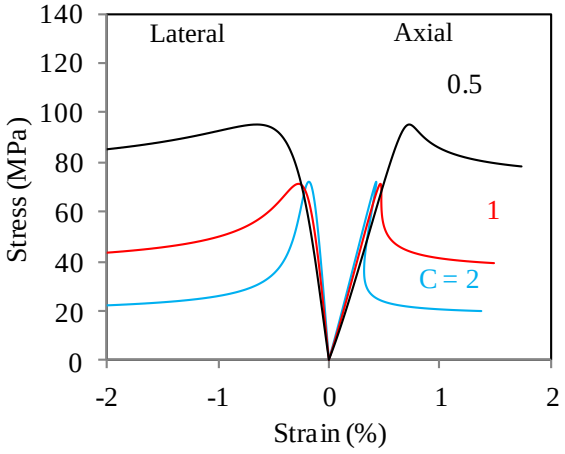

(d) Effects of C

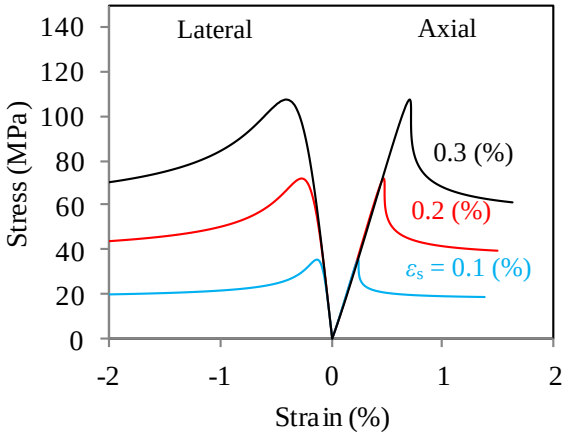

(e) Effects of ε_s

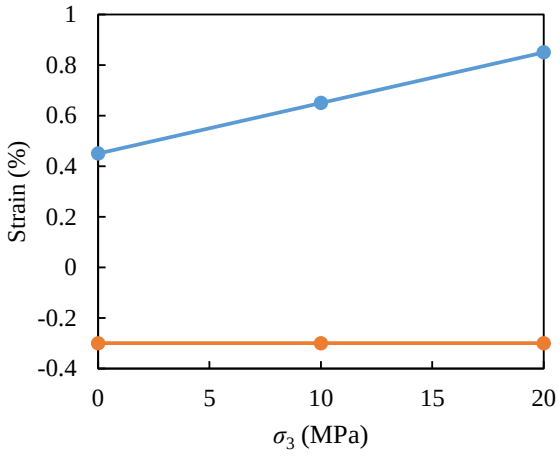

(f) Critical strains

Fig. 1.11 Simulated stress-strain curves. Default values are A = 20 (GPa), k = 0.25, C = 1, ε_s = 0.002, and σ_3 = 0.

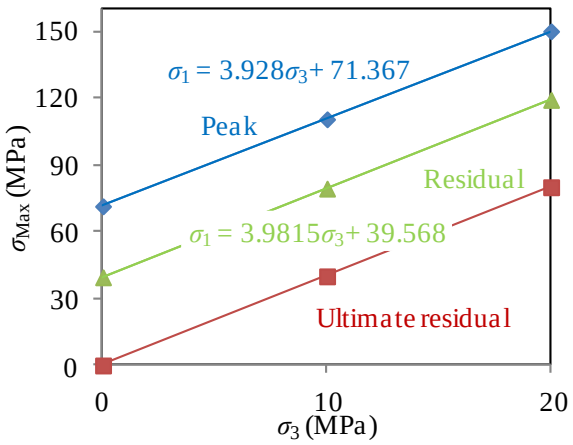

Fig. 1.12 Failure envelopes for Fig. 1.11a.

For comparison, the examples of one conventional 2D elasto-plastic constitutive model (Eqs. 1.26-35, Pourhosseini and Shabanimashcool, 2014) are discussed. The model is complicated and needs eight parameters.

$$f = \sigma_1 - \frac{2c(\eta)\cos\phi}{1-\sin\phi} - \sigma_3\frac{1+\sin\phi}{1-\sin\phi} \tag{1.26}$$

$$c = c_0\left(1 - \frac{\tanh(100\gamma_p)}{\tanh(10)} + 0.001\right)^n \tag{1.27}$$

$$\eta = \gamma_p = \varepsilon_1^p - \varepsilon_3^p \tag{1.28}$$

$$\lambda = \frac{1}{h}\frac{\partial f}{\partial \sigma}\dot{\sigma} \tag{1.29}$$

$$h = -\sqrt{\left[\frac{1}{3}\left(1+\sin(\phi)\sin(\psi)\right)\right]}\frac{\partial f}{\partial \eta} \tag{1.30}$$

$$\dot{\varepsilon}_{ij} = \lambda\frac{\partial g}{\partial \sigma_{ij}} \tag{1.31}$$

$$g = \sigma_1 - \sigma_3\tan\left[\psi\left(\eta,\sigma_3\right)\right] \tag{1.32}$$

$$\Delta\varepsilon^{ps} = \frac{1}{\sqrt{2}}\sqrt{\left(\begin{matrix}\dot{\varepsilon}_1^p\dot{\varepsilon}_1^p + \dot{\varepsilon}_2^p\dot{\varepsilon}_2^p + \dot{\varepsilon}_3^p\dot{\varepsilon}_3^p\end{matrix}\right)} \tag{1.33}$$

$$\psi = \psi_0 \left(1 - \frac{\tanh(100\gamma_p)}{\tanh(10)} + 0.001 \right)^m \tag{1.34}$$

$$\psi_0 = G \ln\left(\frac{\phi\sigma_{ci}}{\sigma_3 + 0.10} \right) - H \tag{1.35}$$

The results, according to Pourhosseini and Shabanimashcool, 2014, including Young's modulus E = 23 GPa, v = 0.135, friction angle ϕ = 49.36, cohesion c_0 = 17.81 MPa, and four fitting parameters: n = 0.29, m = 0.1, G = 7.486, H = 28.351, are represented by the blue lines in Figs. 1.13a and b. However, the 2D simple model needs only four parameters, A = 16.62 GPa, k = 0.18, C = 3.5, and ε_s = 0.002, to approximate the experimental results (Figs. 1.13a and b).

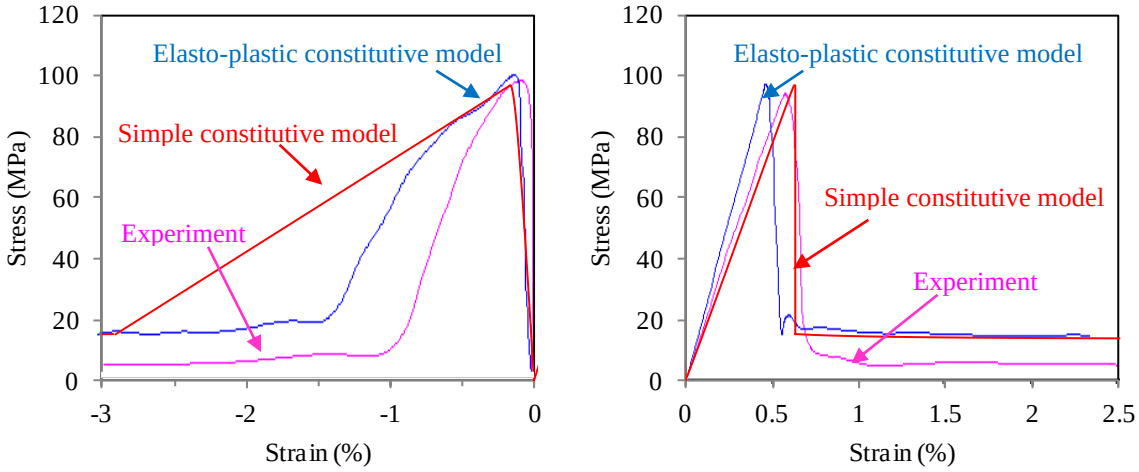

(a) Lateral stress-strain curves (b) Axial stress-strain curves

Fig. 1.13 Stress-strain curves of sandstone under the uniaxial compression.

The simple 2D model by Fujii and Ishijima is better than the variable-compliance-type model because it can simulate the axial stress-lateral strain relationship. The simple 2D model is also simpler than the conventional elasto-plastic model. However, the predicted failure envelope was linear, and the effect of σ_2 was not considered. Therefore, these problems will be solved in the following chapters.

2. Modified 2D model

2.1 Introduction confining pressure-dependent *k*

Confining pressure-dependent *k* (Fig. 2.1a) is introduced to give a convex failure envelope based on the increase in the secant Poisson's ratio with confining pressure under triaxial compression (Fig. 2.1b):

$$k = \frac{\Delta k}{\pi}\left[\tan^{-1}\left\{\frac{1}{\alpha}\left(\sigma_3 - \sigma_0\right)\right\} + \frac{\pi}{2}\right] + k_0 \tag{2.1}$$

where k_0 is the minimum value, Δk is the amplitude, and σ_0 and α are constants. The ultimate residual strength is unchanged from Eq. 1.25.

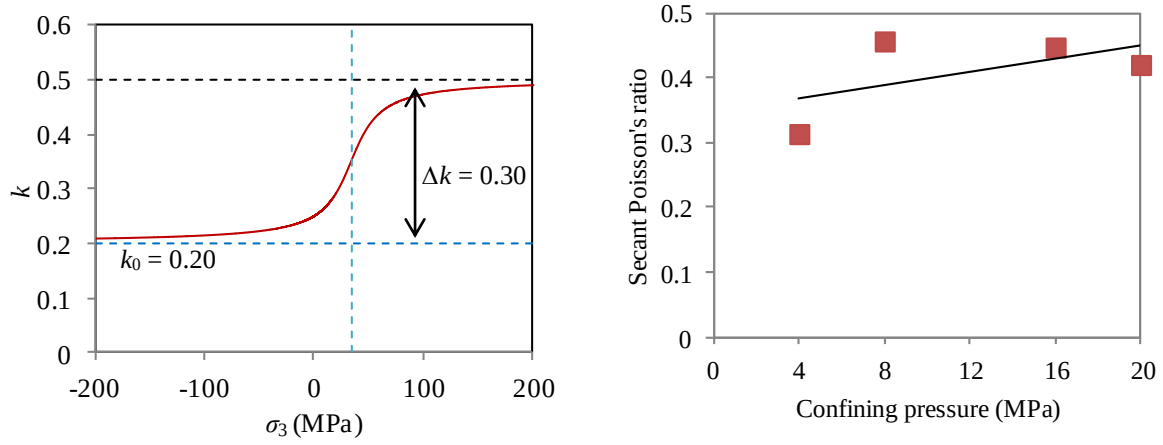

(a) (b)

Fig. 2.1 (a): Confining pressure-dependent *k* where k_0 = 0.20, σ_0 = 35 MPa, α = 20 MPa, and Δk = 0.30. (b): Secant Poisson's ratio increases with confining pressure for Kamisunagawa sandstone (Fujii and Ishijima, 1998).

The stress–strain curves obtained by setting default values of *A* = 20 GPa, *C* = 1, ε_s = 0.002, k_0 = 0.20, σ_0 = 35 MPa, α = 20 MPa, and Δk = 0.30 show strain-softening behaviors (Fig. 2.2a) with a convex failure envelope (Fig. 2.2b). The stress drop decreases, and the strain-softening behavior becomes mild as confining pressure increases; these are common features of rock deformation. Figure 2.2b also shows the failure envelope predicted by the Hoek–Brown strength criterion with σ_c = 71.6 MPa, m_b = 119.0, *s* = 1, and α = 0.104, which is similar. Therefore, the equations are expected to approximate the stress–strain curves and convex failure envelope of various rocks.

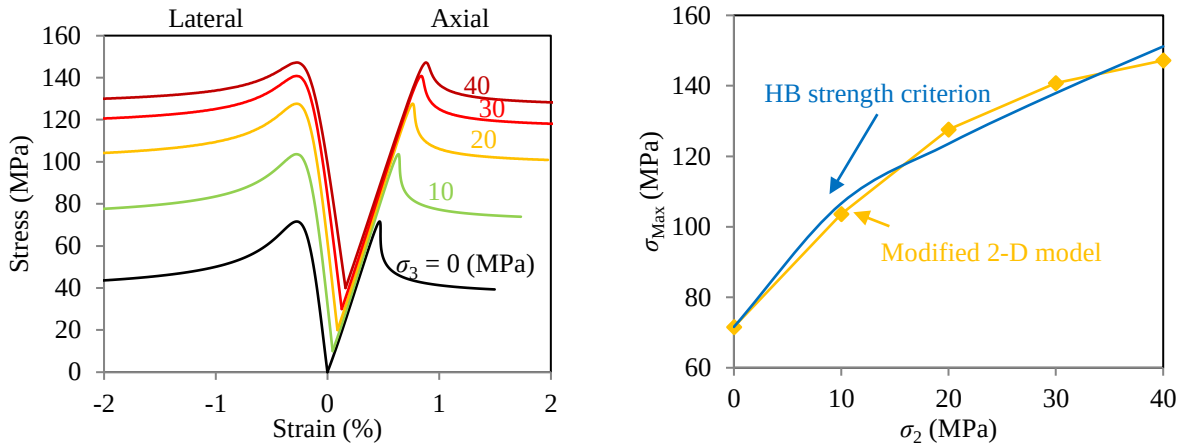

(a) Stress-strain curves

(b) Failure envelope

Fig. 2.2 Stress-strain curves.

The constant k_0 mainly affects the maximum stress and the post-failure behavior (Fig. 2.3). The constant Δk (Fig. 2.4) and σ_0 (Fig. 2.5) mainly affect the internal friction angle. The constant α mainly affects the convexity of the failure envelope (Fig. 2.6).

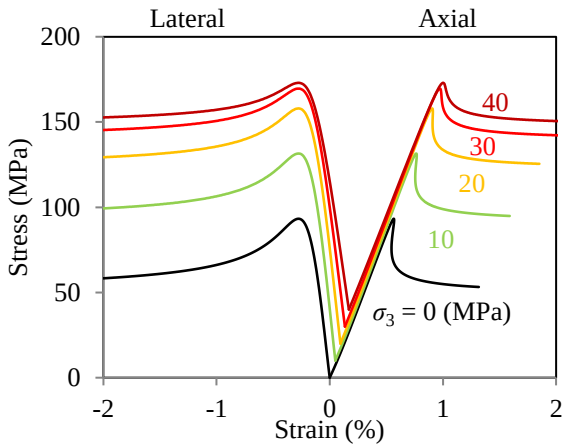

(a) k_0 = 0.15

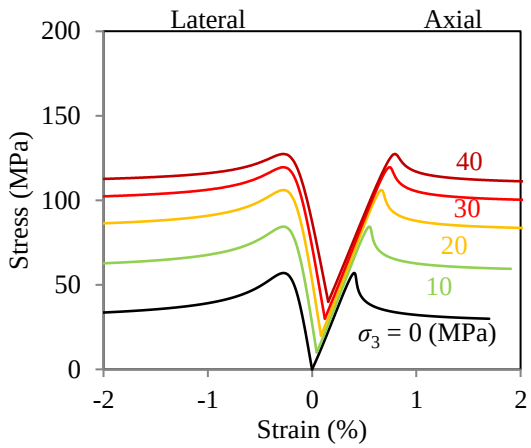

(b) k_0 = 0.25

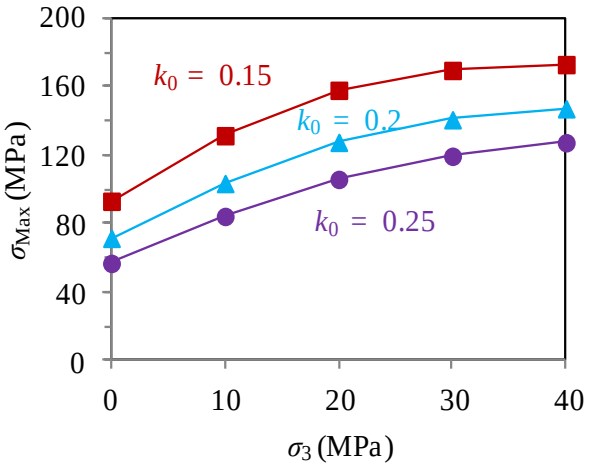

(c) Failure envelope

Fig. 2.3 Effect of k_0 on the stress-strain curves.

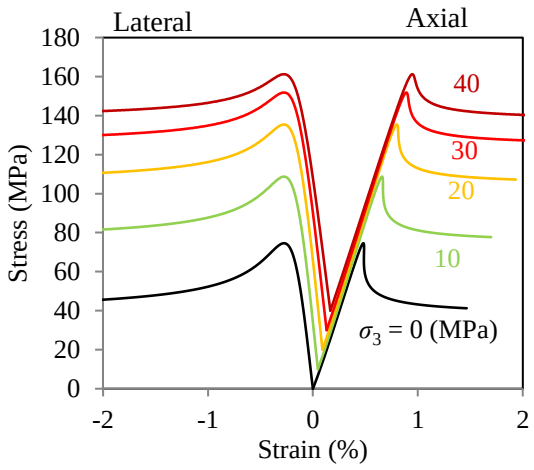

(a) Δk = 0.25

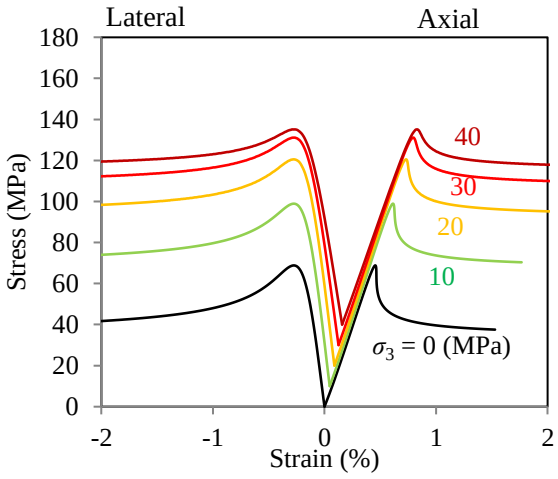

(b) Δk = 0.35

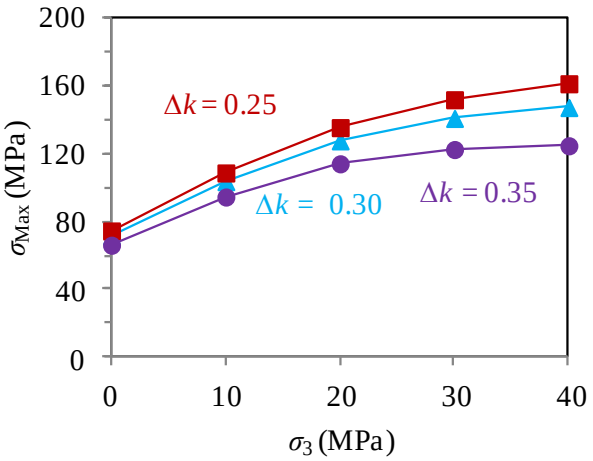

(c) Failure envelope

Fig. 2.4 Effect of Δk on the stress-strain curves.

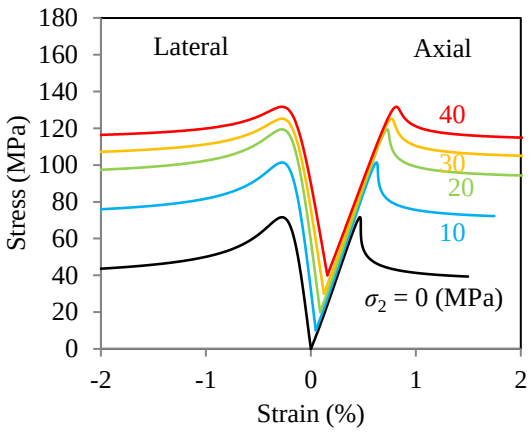

(a) σ_0 = 28 (MPa)

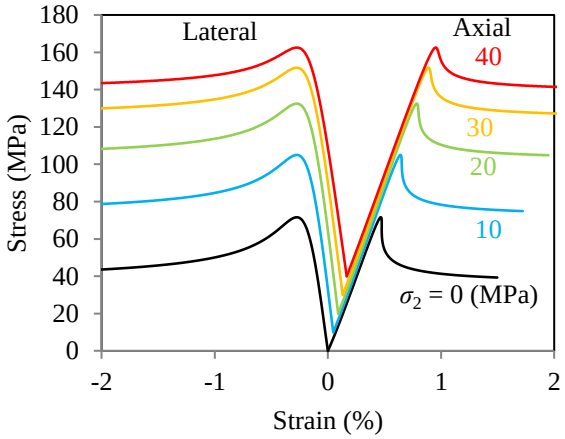

(b) σ_0 = 42 (MPa)

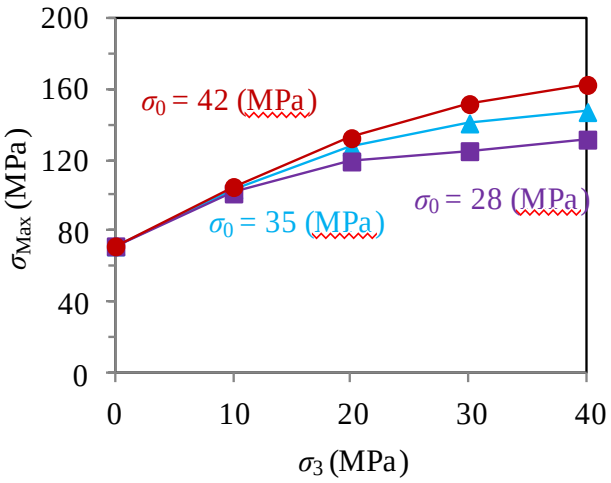

(c) Failure envelope

Fig. 2.5 Effect of σ_s on the stress-strain curves.

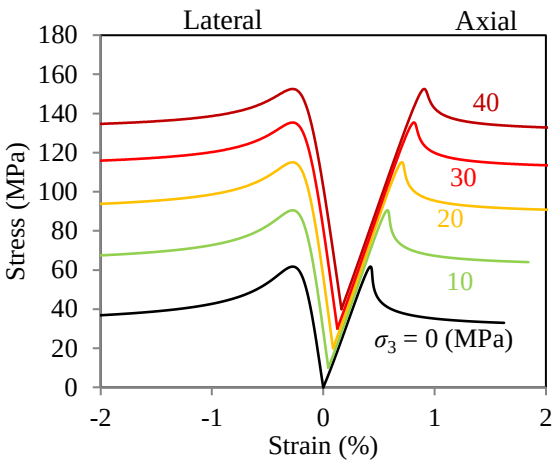

(a) α = 20 MPa

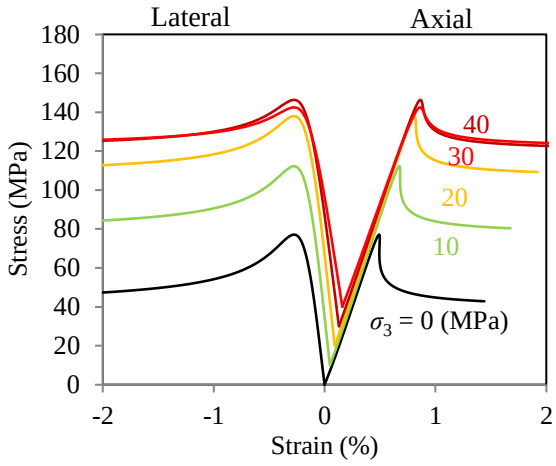

(b) α = 40 MPa

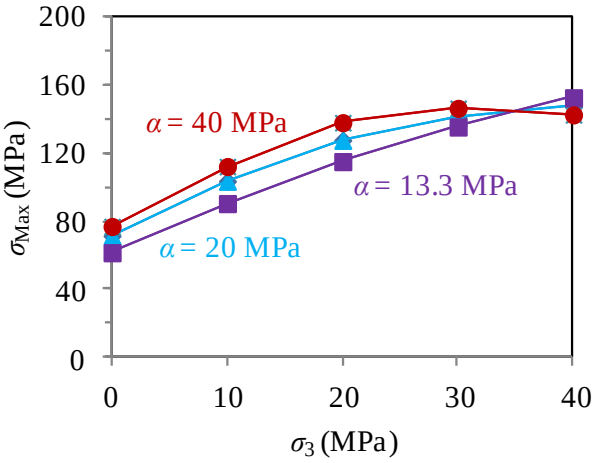

(c) Failure envelope

Fig. 2.6 Effect of α on the stress-strain curves.

2.2 Approximating convex failure envelope for test results

The procedure for approximating ordinary triaxial experimental data using the modified 2D model is as follows:

(b1) Adjust A to approximate the gradient of the stress–strain curve,

(b2) Adjust C to approximate the overall shape of each stress–strain curve,

(b3) Adjust ε_s to approximate the peak load point and slope of the failure envelope,

(b4) Adjust k to approximate the gradient of the axial stress–lateral strain curve and peak strength,

(b5) Iterate steps (b1−b4) until the stress–strain curves for the rocks are approximated well,

(b6) Adjust k to approximate the peak strength for the triaxial compression test, and

(b7) Use a nonlinear least squares method for the k vs. σ_3 curve to obtain values of k_0, Δk, α, and σ_0 (e.g., Figs. 2.7, 2.13b, and 2.14b).

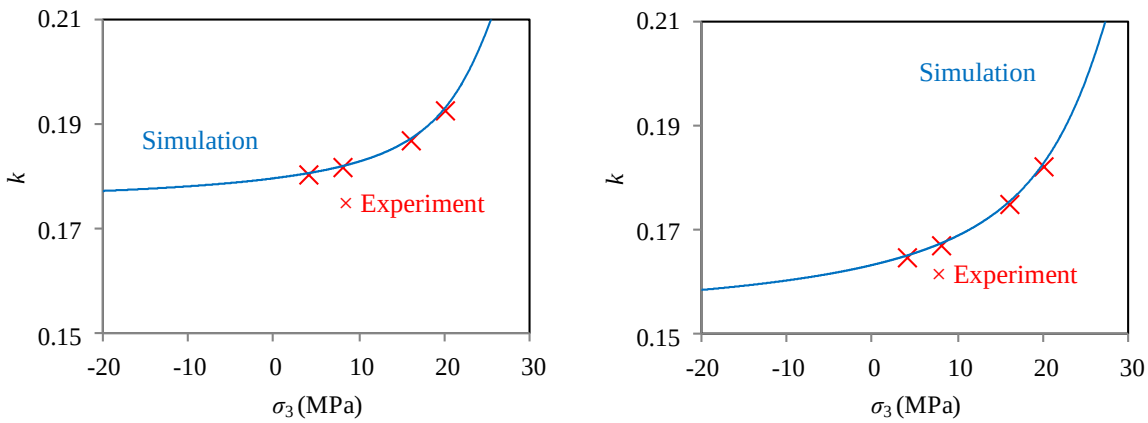

Fig. 2.7 k vs. σ_3 for (a): A = 13 (GPa), C = 0.4, and ε_s = 0.002. (b): A = 13 (GPa), C = 3.5, and ε_s = 0.0025.

Results for at least three different values of confining pressure are needed for these approximations. Two parameter sets were used to approximate the stress–strain curves of Kamisunagawa sandstone in Fujii and Ishijima (1998). The results from the first parameter set mainly focused on approximating the stress–strain behavior up to the peak load points (Fig. 2.8). The peak strength was well approximated; however, the residual strength was not (Fig. 2.8). The results from the second parameter set mainly focused on the stress–strain behavior from the peak load points to the residual strength (Fig. 2.10). The calculation is

lateral strain-controlled, but the experiment was axial strain-controlled; therefore, the dashed red lines in Fig. 2.10 must be compared with experimental results. The peak and residual strengths were well approximated (Fig. 2.10).

Currently, the modified 2D model cannot simultaneously approximate the shape around the peak load point and the post-peak behavior. However, considering that rock masses are fractured, the simulation focusing on the post-peak behavior (Fig. 2.10) is more helpful in understanding the rock failure process (Zhao and Cai, 2010; Yang et al., 2012) and designing rock structures (Bruning et al., 2018). Therefore, the post-peak behavior in the rest of this paper is prioritized approximating.

The difference between the predicted and observed strains (Figs. 2.8 and 2.10) is mainly due to ignorance of the initial strain values. Introducing one or two constants would solve this problem; however, the model's simplicity is maintained.

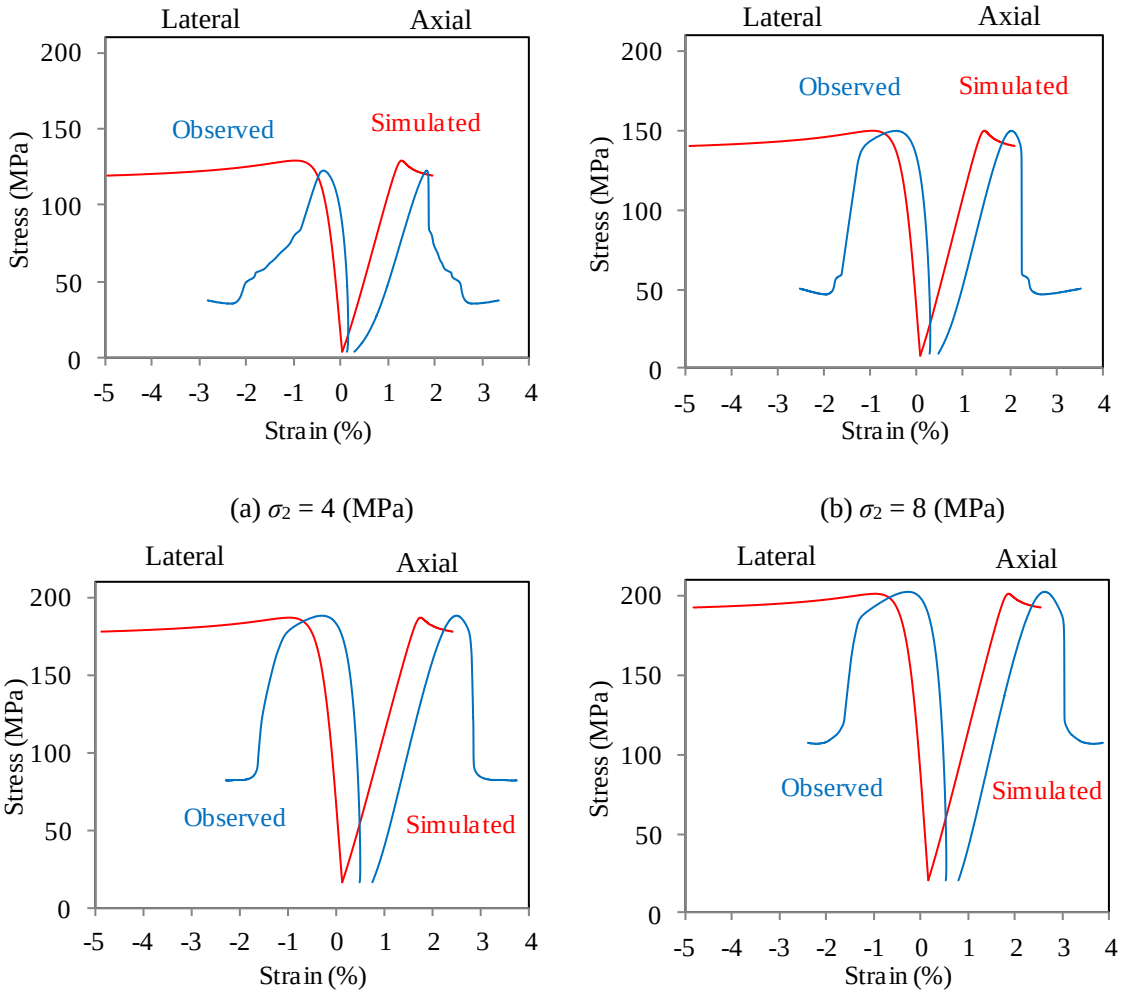

(a) σ_2 = 4 (MPa)

(b) σ_2 = 8 (MPa)

(c) σ_2 = 16 (MPa)

(d) σ_2 = 20 (MPa)

Fig. 2.8 Observed and approximated stress-strain curves of Kamisunagawa sandstone under the ordinary triaxial compression by A = 13 (GPa), C = 0.4, ε_s = 0.002, k_0 = 0.174, Δk = 0.0813, α = 5.86 (MPa), and σ_0 = 26.6 (MPa).

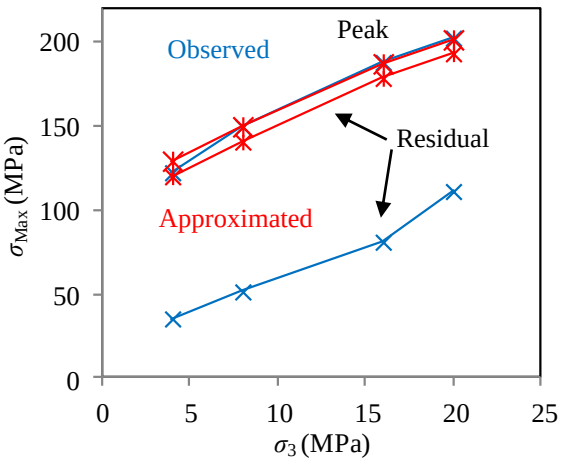

Fig. 2.9 Failure envelopes for Fig. 2.8.

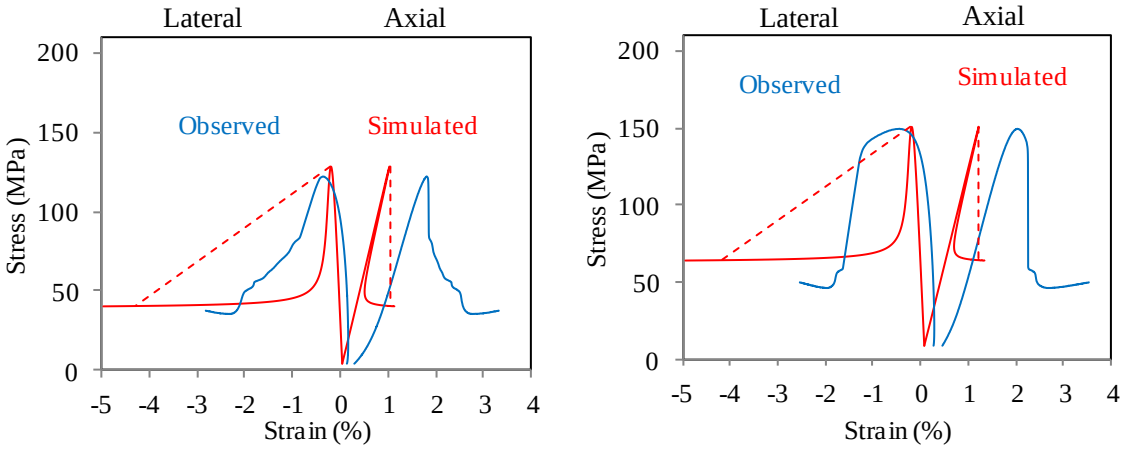

(a) σ_2 = 4 (MPa)

(b) σ_2 = 8 (MPa)

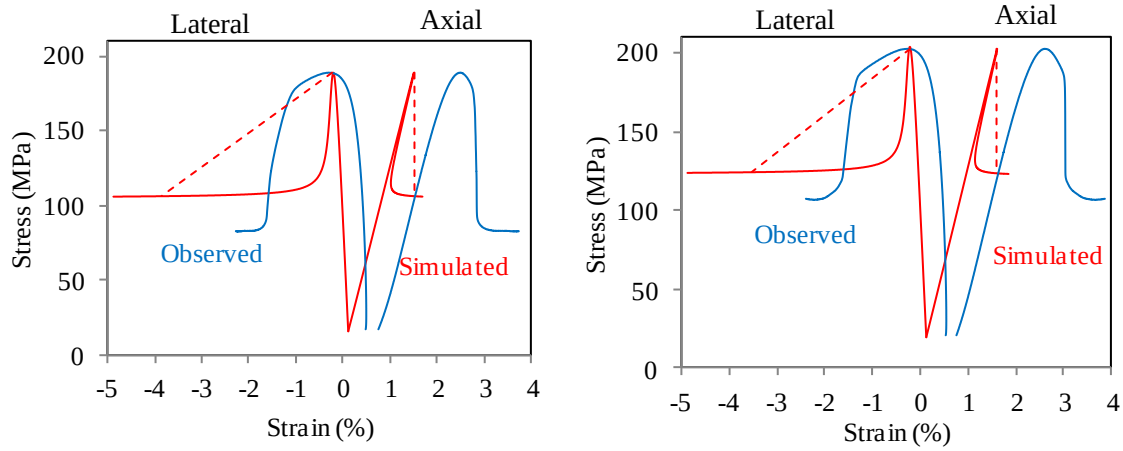

(c) σ_2 = 16 (MPa)

(d) σ_2 = 20 (MPa)

Fig. 2.10 Observed and approximated stress-strain curves of Kamisunagawa sandstone under the ordinary triaxial compression by A = 13 (GPa), C = 3.5, ε_s = 0.0025, k_0 = 0.151, Δk = 0.152, α = 7.77 (MPa), and σ_0 = 30.3 (MPa).

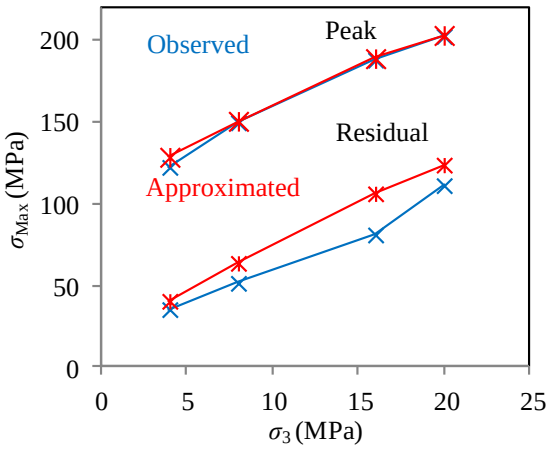

Fig. 2.11 Failure envelopes for Fig. 2.10.

2.3 Comparison with other 2D models

For comparison, the examples of two conventional 2D elasto-plastic constitutive models (Fig. 2.12a, Zhang, 2018; Fig. 2.12b, Zhang, et al., 2013) are discussed. These models are complicated and need 11 and 10 parameters to approximate the experimental stress–strain curves.

The results, according to Zhang (2018), including elastic (E_0 = 45.51 GPa and ν_0 = 0.320), strength (α_1 = 2.07, κ = 34.5 MPa, and α_2 = 2.07), plastic hardening (h_0 = 0.58, h_1 = 1.40, and b = 900), damage (ω_c = 0.70, β_1 = 0.50 MPa^{-1}, r = 0.2), and damage softening (a = 3.45 exp[−0.047σ_3]) parameters, are represented by the black lines in Fig. 2.13a.

The results, according to Zhang, et al. (2013), including elastic (bulk modulus, K_0 = 8 GPa; shear modulus initial value, G_0 = 6 GPa; shear modulus residual value, G_r = G_0 × 0.8) and plastic (friction angle plastic internal variable threshold, P_ϕ = 0.4; friction angle initial value, ϕ_0 = 18°; friction angle residual value, ϕ_r = 34.5°; shear dilatancy angle initial value, ψ_0 = 25°; shear dilatancy angle residual value, ψ_r = 10°; cohesion initial value c_0 = 15 MPa; cohesion residual value c_r = 9.0 MPa) parameters, and a plastic internal variable (2.5σ_3 / σ_c + 0.27) are represented by the black lines in Fig. 2.14a.

$$\varepsilon = \varepsilon^e + \varepsilon^p$$

$$d\varepsilon = d\varepsilon^e + d\varepsilon^p$$

$$\sigma = \frac{\partial \phi^e}{\partial \varepsilon^e} = D : \varepsilon^e$$

$$\omega = 1 - \frac{E}{E_0}$$

$$R = \frac{\partial \phi^p}{\partial \gamma^p}$$

$$Y = \frac{\partial \phi}{\partial \omega} = r\frac{\partial \phi^e}{\partial \omega} + (1-r)\frac{\partial \phi^p}{\partial \omega}$$

$$= rY^e + (1-r)Y^p$$

$$d\gamma^p = d\lambda^p \frac{\partial G^p}{\partial \sigma}$$

$$d\gamma^p = d\lambda^p \frac{\partial G^p}{\partial R}$$

$$d\omega = d\lambda^\omega \frac{\partial G^\omega}{\partial Y}$$

$$\phi^e\left(\varepsilon^e,\ \omega\right) = \frac{1}{2}\ \varepsilon^e : D\ :\ \varepsilon$$

$$\gamma^p = \int d\gamma^p = \int \sqrt{2\, de^p :\ de^p / 3}$$

$$dF^p = \frac{\partial F^p}{\partial \sigma} : d\sigma + \frac{\partial F^p}{\gamma^p} + \frac{\partial F^p}{\partial \omega} d\omega = 0$$

$$F^p = g(\theta)\, q + \alpha_1\ p - \chi^{pw}\kappa = 0$$

$$\chi^{pw} = \left[h_1 - (h_1 - h_0)\exp(b\gamma^p)\right] - (1-\omega)$$

$$dF^\omega = \frac{\partial F^\omega}{\partial Ye} dY^e + \frac{\partial F^\omega}{\partial Y^p} dY^p + \frac{\partial F^\omega}{\partial \omega} d\omega = 0$$

$$F^\omega = \omega_c - \omega_c \exp(\beta Y) - \omega =$$

$$d\lambda^\omega = \frac{\partial F^\omega}{\partial Y^e} \varepsilon^e :\ D_0 :\ d\varepsilon\ /\ H^\omega$$

$$H^\omega = \frac{\partial F^\omega}{\partial \omega}\frac{\partial G^\omega}{\partial Y^e}$$

$$d\sigma = D^{e\omega} :\ d\varepsilon$$

$$D^{e\omega} = D - \frac{\partial G^\omega}{\partial Y^e}\frac{\partial F^\omega}{\partial Y^e}(D_0 : \varepsilon^e) \otimes (\varepsilon^e : D_0) / H^\omega$$

(a) A 2D conventional elasto-plastic constitutive model (Zhang, 2018)

$$d\varepsilon_{ij} = d\varepsilon_{ij}^{\ R} + d\varepsilon_{ij}^{\ I} + \varepsilon_{ij}^{\ C}$$

$$d\varepsilon_{ij}^{\ I} = d\varepsilon_{ij}^{\ p} + d\varepsilon_{ij}^{\ C}$$

$$d\varepsilon_{ij}^{\ C} = \frac{\partial C_{ijkl}(P)}{\partial P} dP \bullet \sigma_{kl}$$

$$d\sigma_{ij} = C_{ijkl}(P)(d\varepsilon_{ij} - d\varepsilon_{ij}^{\ I})$$

$$P = \int dP, dP = \frac{d\gamma^p}{f(\sigma_3 / \sigma_c)}$$

$$f(\sigma_3 / \sigma_c) = a \bullet \sigma_3 / \sigma_c + b$$

$$d\varepsilon_{ij}^I = \lambda \frac{\partial g}{\partial \sigma_{ij}}$$

$$d\gamma^p = \sqrt{\frac{2}{3} de_{ij}^p \bullet de_{ij}^p}$$

$$de_{ij}^p = d\varepsilon_{ij}^p - \frac{1}{3} d\varepsilon_{kk}^p \delta_{ij}$$

$$\sigma_1 = \frac{2c\cos\varphi}{1-\sin\varphi} + \sigma_3 \frac{1+\sin\varphi}{1-\sin\varphi}$$

$$g = \sigma_1 - \sigma_3 \tan^2\left(45 + \frac{\psi}{2}\right) - 2c\tan\left(45 + \frac{\psi}{2}\right)$$

$$\psi = \arcsin\frac{(d\varepsilon_1^p + 2d\varepsilon_3^p) + (d\varepsilon_1^C + 2\varepsilon_3^C)}{(d\varepsilon_1^p - 2d\varepsilon_3^p) + (d\varepsilon_1^C - 2\varepsilon_3^C)}$$

(b) Another example (Zhang et al., 2013)

Fig. 2.12 Examples of two conventional 2D elasto-plastic constitutive models.

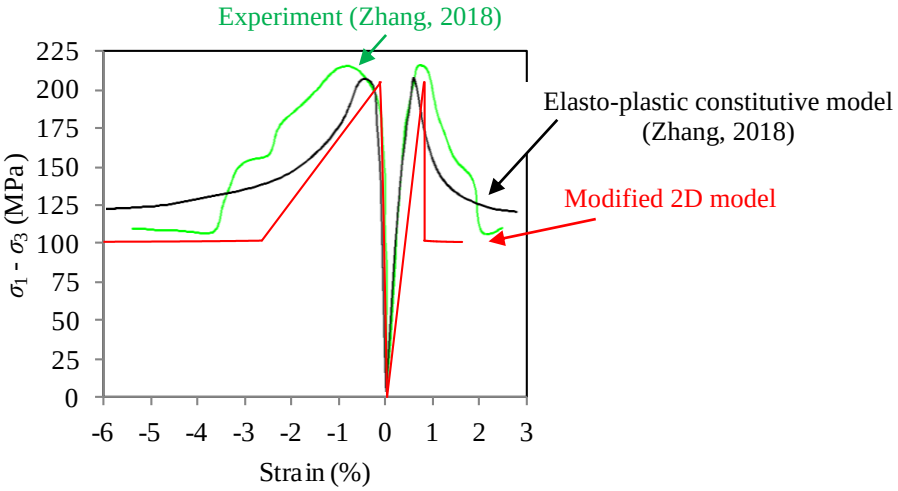

(a) Stress-strain curves

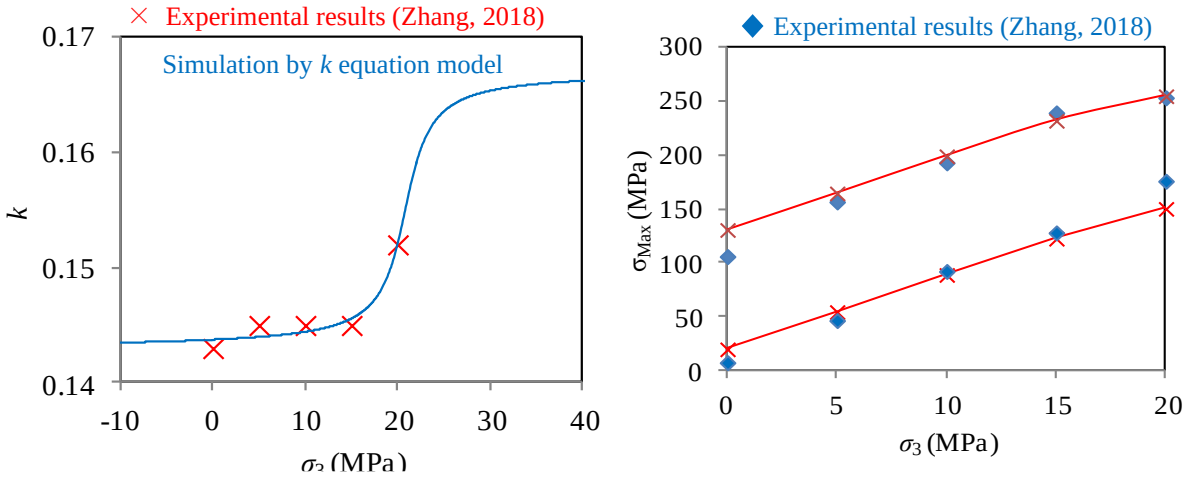

(b) k vs. σ_3 (c) Failure envelopes

Fig. 2.13 (a): Stress-strain curves of limestone under σ_3 = 15 (MPa). (b): k vs. σ_3 for parameter A = 27 (GPa), C = 3.5, and ε_s = 0.0013. (c): Approximated convex failure envelopes by modified 2D model.

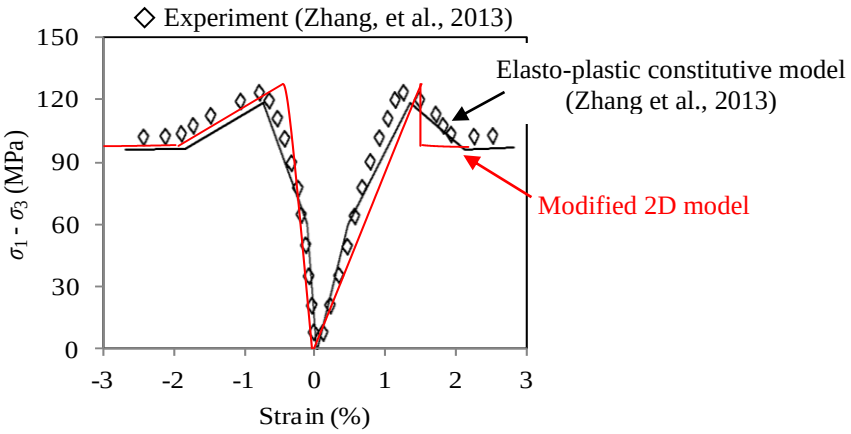

(a) Stress-strain curves

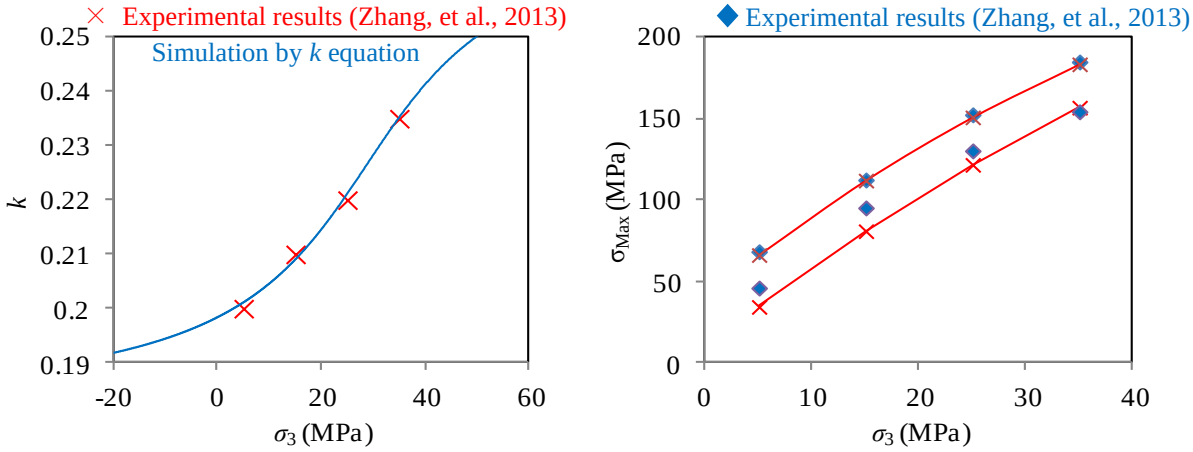

(b) k vs. σ_3 (c) Failure envelope

Fig. 2.14 (a): Stress-strain curves of red sandstone under σ_3 = 25 (MPa). (b): k vs. σ_3 for parameter A = 9 (GPa), C = 2.5, and ε_s = 0.002. (c): Approximated convex failure envelopes by modified 2D model.

The two models simulate the experimental stress–strain curves well. However, the models can neither simulate tensile failure nor consider the critical strains, and they both approximate failure envelopes as linear.

The modified 2D model's approximated stress–strain curves and convex failure envelopes are also shown in Figs. 2.13 and 2.14. For limestone, the parameters A = 27 GPa, C = 3.5, and ε_s = 0.0013 were given, and the parameters k_0 = 0.143, Δk = 0.0239, α = 2.04 MPa, and σ_0 = 20.9 MPa were obtained by a nonlinear least-squares method (Fig. 2.13b). For red sandstone, the parameters A = 9 GPa, C = 2.5, and ε_s = 0.002 were given, and the parameters k_0 = 0.18, Δk = 0.0928, α = 20.6 MPa, and σ_0 = 29.0 MPa were obtained by

a nonlinear least-squares method (Fig. 2.14b). The stress–strain curves (Figs. 2.13a and 2.14a) and convex failure envelopes (Figs. 2.13c and 2.14c) for rocks are simulated well.

Among these three models, the modified 2D model is the best because it can approximate the stress–strain curves as precisely as the others but with fewer equations and parameters.

2.4 Example application

As an example of its application, the stress distribution of a pressurized thick-walled cylinder with inner and outer radii r_1 and r_2, respectively, under internal and external pressures P_1 and P_2, respectively, was calculated, using the simple 2D model assuming the plane strain condition (Fig. 2.15). The following process of calculation (Eqs. 2.2-2.9) was carried out by an axisymmetric finite element method (FEM), dividing the radial axis from 1 to 19 m into 470 elements and from 19 to 100 m into 320 elements.

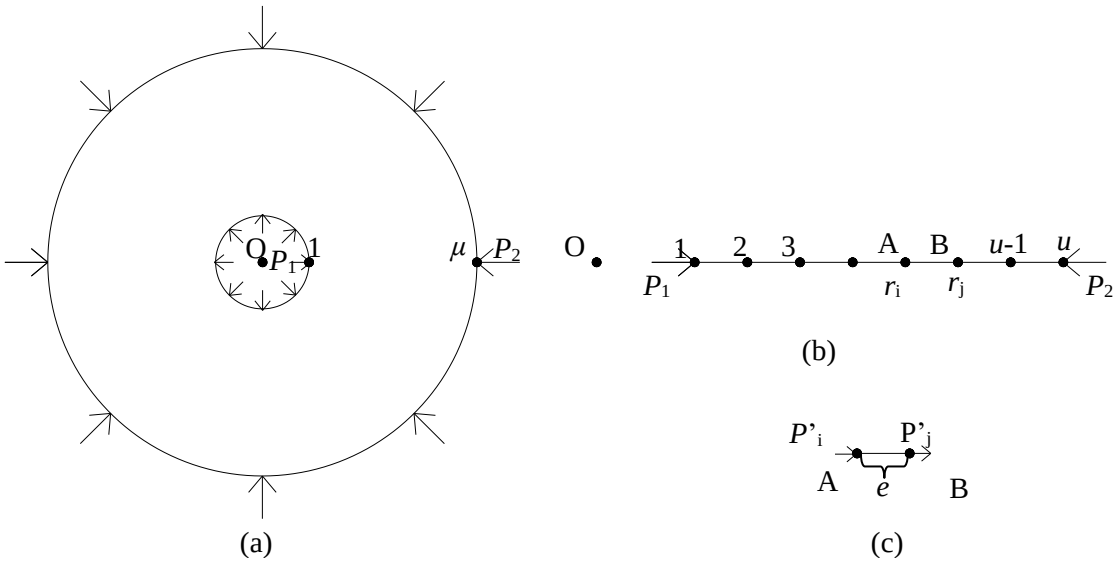

Fig. 2.15 (a): Thick-walled cylinder. (b): Element division. (c): An element.

The radial and tangential stress σ_r and σ_θ are,

$$\begin{Bmatrix} \sigma_\theta \\ \sigma_r \end{Bmatrix} = \begin{bmatrix} \frac{r_m}{e} & \frac{r_m}{e} \\ -\frac{1}{2} & \frac{1}{2} \end{bmatrix} \begin{Bmatrix} P'_i \\ P'_j \end{Bmatrix} \tag{2.2}$$

where e is the length of the element, r_m is the mean radius of r_i and r_j, and P is the nodal force. Then, the radial and tangential strains ε_r and ε_θ will be,

$$\begin{Bmatrix} \varepsilon_r \\ \varepsilon_\theta \end{Bmatrix} = \begin{bmatrix} A(\varepsilon_r) & kA \\ kA & A(\varepsilon_\theta) \end{bmatrix}^{-1} \begin{Bmatrix} \sigma_\theta \\ \sigma_r \end{Bmatrix} \tag{2.3}$$

The displacement u_i and u_j are,

$$\begin{Bmatrix} u_i \\ u_j \end{Bmatrix} = \begin{bmatrix} r_i & -e/2 \\ r_j & +e/2 \end{bmatrix} \begin{Bmatrix} \varepsilon_\theta \\ \varepsilon_r \end{Bmatrix} \tag{2.4}$$

Substituting Eqs. 2.2 and 2.3 into Eq. 2.4,

$$\begin{Bmatrix} u_i \\ u_j \end{Bmatrix} = \begin{bmatrix} r_i & -e/2 \\ r_j & +e/2 \end{bmatrix} \begin{bmatrix} A(\varepsilon_r) & kA \\ kA & A(\varepsilon_\theta) \end{bmatrix}^{-1} \begin{bmatrix} \frac{r_m}{e} & \frac{r_m}{e} \\ -\frac{1}{2} & \frac{1}{2} \end{bmatrix} \begin{Bmatrix} P'_i \\ P'_j \end{Bmatrix} \tag{2.5}$$

Then, the nodal force P'_i and P'_j can be written as

$$\begin{Bmatrix} P'_i \\ P'_j \end{Bmatrix} = R \begin{Bmatrix} u_i \\ u_j \end{Bmatrix} \tag{2.6}$$

$$R = \left\{ \begin{bmatrix} r_i & -e/2 \\ r_j & +e/2 \end{bmatrix} \begin{bmatrix} \frac{A(\varepsilon_\theta)}{A(\varepsilon_\theta)\times A(\varepsilon_r) - (kA)^2} & \frac{-kA}{A(\varepsilon_\theta)\times A(\varepsilon_r) - (kA)^2} \\ \frac{-kA}{A(\varepsilon_\theta)\times A(\varepsilon_r) - (kA)^2} & \frac{A(\varepsilon_r)}{A(\varepsilon_\theta)\times A(\varepsilon_r) - (kA)^2} \end{bmatrix} \begin{bmatrix} \frac{r_m}{e} & \frac{r_m}{e} \\ -\frac{1}{2} & \frac{1}{2} \end{bmatrix} \right\}^{-1} \tag{2.7}$$

The total nodal P'_1, P'_2… and P'_u at point 1, 2…and 790 are as follows,

$$\left.\begin{aligned} P'_1 &= P_{A1} \\ P'_2 &= P_{B1} + P_{A2} \\ P'_3 &= P_{B2} + P_{A3} \\ &\\ P'_u &= P_{B(u-1)} \end{aligned}\right\} \tag{2.8}$$

From Eqs. 2.3 to 2.8, the total nodal force can be written as

$$\begin{Bmatrix} P_1 \\ 0 \\ \cdot \\ 0 \\ -P_2 \end{Bmatrix} = \begin{bmatrix} a_{11} & a_{12} & 0 & \cdot & 0 \\ a_{21} & a_{22} & a_{23} & \cdot & 0 \\ 0 & a_{32} & a_{33} & \cdot & \cdot \\ \cdot & \cdot & \cdot & \cdot & \cdot \\ 0 & 0 & \cdot & a_{uu-1} & a_{uu} \end{bmatrix}^{\mathrm{T}} \begin{Bmatrix} u_1 \\ u_2 \\ \cdot \\ \cdot \\ u_{\mathrm{u}} \end{Bmatrix} \tag{2.9}$$

where a_{ij} is a coefficient.

The results were compared to Bray's analytical elasto-plastic solution (Goodman, 1980) by the following equations (Eqs. 2.10-2.17) for a circular hole in an infinite elasto-brittle material (Fig. 1.1c). The modified 2D model was not used because Bray's solution was only for a linear failure envelope and thus cannot be compared.

Within the elastic zone, the stress σ_r and σ_θ are,

$$\sigma_r = P_2 - \frac{b}{r^2} \tag{2.10}$$

$$\sigma_\theta = P_2 + \frac{b}{r^2} \tag{2.11}$$

$$b = \left[\frac{\left\{ \tan^2\left(45 + \frac{\varphi}{2}\right) - 1 \right\} P_2 + q_{\mathrm{u}}}{\tan^2\left(45 + \frac{\varphi}{2}\right) + 1} \right] R^2 \tag{2.12}$$

$$R = r_1 \left[\frac{2P_2 - q_{\mathrm{u}} + \left\{ 1 + \tan^2\left(45 + \frac{\varphi_{\mathrm{j}}}{2}\right) \right\} S_j \cot\varphi_{\mathrm{j}}}{\left\{ 1 + \tan^2\left(45 + \frac{\varphi_{\mathrm{j}}}{2}\right) \right\} (P_1 + S_{\mathrm{j}} \cot\varphi_{\mathrm{j}})} \right]^{\frac{1}{Q}} \tag{2.13}$$

$$Q = \frac{\tan\delta}{\tan(\delta - \varphi_{\mathrm{j}})} - 1 \tag{2.14}$$

$$\delta = 45 + \frac{\varphi_{\mathrm{j}}}{2} \tag{2.15}$$

Within the plastic zone, the stress σ_r and σ_θ were written as,

$$\sigma_r = (P_1 + S_j \cot \varphi_j)\left(\frac{r}{r_1}\right)^Q - S_j \cot \varphi_j \tag{2.16}$$

$$\sigma_\theta = (P_1 + S_j \cot \varphi_j)\frac{\tan \delta}{\tan(\delta - \varphi_j)}\left(\frac{r}{r_1}\right)^Q - S_j \cot \varphi_j \tag{2.17}$$

Parameters that were the same as for Fig. 1.11a and 1.12 (A = 20 GPa, k = 0.25, C = 1, ε_s = 0.002) were used for the simple 2D model. The uniaxial compressive strength q_u = 71.4 MPa, internal friction angle ϕ = 36.5°, friction angle for the residual strength ϕ_j = 36.9°, E = 14.5 GPa, ν = 0.270, and residual cohesion S_j = 9.89 MPa were used for Bray's solution. The parameters were obtained from Fig. 1.11a and 1.12.

Plastic zones can be seen for both models (Fig. 2.16a). The decrease in strain-dependent elastic modulus (Fig. 2.16b) around the opening induced a tangential stress decrease for the simple 2D model. The results from Bray's solution appear somewhat angular when plotted, while the results of the simple 2D model are more rounded, reflecting the difference in the stress–strain relationship. The inward displacement by the simple 2D model (Fig. 2.16c) rapidly increases near the inner wall. This rapid increase may represent the dilatancy of rock failure better than Bray's solution, which is based on the rupture plane slip in the plastic zone.

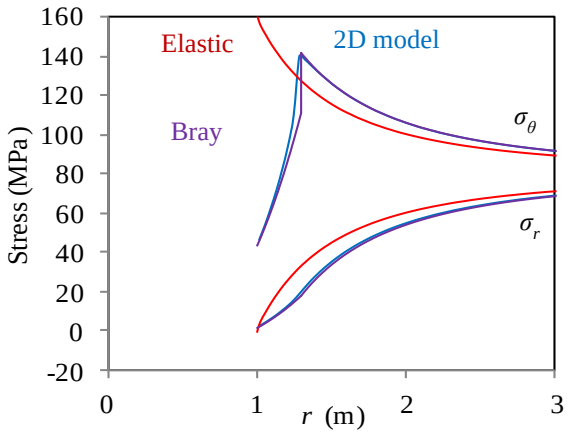

(a) Stress distribution

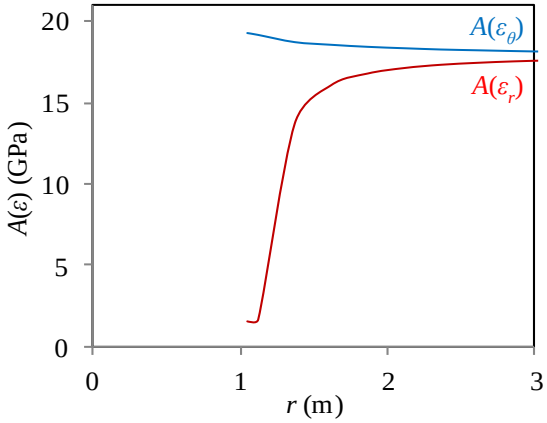

(b) $A(\varepsilon_r)$ and $A(\varepsilon_\theta)$

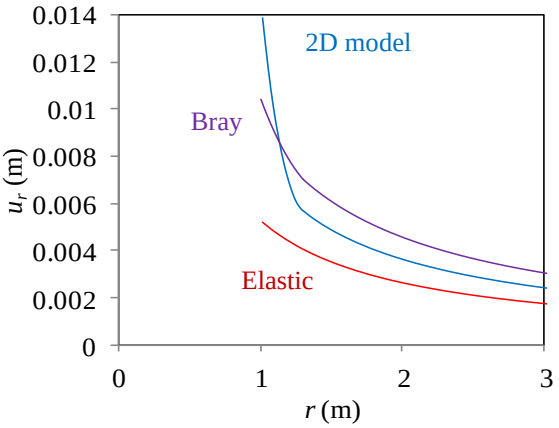

(c) Inward displacement

Fig. 2.16 Calculation results for a hollow cylinder. Parameters for the simple 2D model and that for Bray's analytical elasto-plastic solution are the same as for Fig. 1.11a (A = 20 (GPa), k = 0.25, C = 1, ε_s = 0.002), r_1 = 1 m and r_2 = 100 m, and P_1 = 1 (MPa) and P_2 = 80 (MPa). u_r is the inward displacement by excavation and application of P_1.

3. Simple 3D model

The following simple 3D constitutive model is proposed:

$$\sigma_1 = A(\varepsilon_1)\varepsilon_1 + kA\varepsilon_2 + kA\varepsilon_3 \tag{3.1}$$

$$\sigma_3 = kA\varepsilon_1 + kA\varepsilon_2 + A(\varepsilon_3)\varepsilon_3 \tag{3.2}$$

$$\varepsilon_2 = \frac{\sigma_1 - \sigma_2}{\sigma_1 - \sigma_3}\varepsilon_3 + \frac{\sigma_2 - \sigma_3}{\sigma_1 - \sigma_3}\varepsilon_1 \tag{3.3}$$

Equations 3.1 and 3.2 are based on Eqs. 1.14 and 1.15 for the 2D model. Equation 3.3 is just an elastic equation. The same strain-dependent elastic modulus $A'(\varepsilon)$ is used as in Eq. 1.16,

$$A'(\varepsilon) = D\left[\tan^{-1}\left\{C\left(\frac{\varepsilon}{\varepsilon_s} + 1\right)\right\} + \frac{\pi}{2}\right] + F \tag{3.4}$$

and the terms D and F are chosen so that the residual strength becomes constant for infinite axial compression and lateral expansion (similar to the 2D model) as follows.

It is assumed

$$A'(\varepsilon_1 = \infty) = A \tag{3.5}$$

As ε_3 tends to -∞,

$$A'(\varepsilon_3 = -\infty) = F \tag{3.6}$$

Substituting Eqs. 3.3, 3.5, and 3.6 into Eqs. 3.1 and 3.2,

$$\sigma_3(\varepsilon_1 = \infty, \varepsilon_3 = -\infty) = F\varepsilon_3 + kA\left(\frac{\sigma_1 - \sigma_2}{\sigma_1 - \sigma_3}\varepsilon_3 + \frac{\sigma_2 - \sigma_3}{\sigma_1 - \sigma_3}\varepsilon_1\right) + kA\varepsilon_1 \tag{3.7}$$

$$\sigma_1(\varepsilon_1 = \infty, \varepsilon_3 = -\infty) = A\varepsilon_1 + kA\left(\frac{\sigma_1 - \sigma_2}{\sigma_1 - \sigma_3}\varepsilon_3 + \frac{\sigma_2 - \sigma_3}{\sigma_1 - \sigma_3}\varepsilon_1\right) + kA\varepsilon_3 \tag{3.8}$$

Substituting Eq. 3.7 into Eq. 3.8,

$$\sigma_1(\varepsilon_1 = \infty, \varepsilon_3 = -\infty) = H\varepsilon_1 + \frac{kA\left(1 + \dfrac{\sigma_1 - \sigma_2}{\sigma_1 - \sigma_3}\right)}{kA\dfrac{\sigma_1 - \sigma_2}{\sigma_1 - \sigma_3} + F}\sigma_3 \tag{3.9}$$

where,

$$H = A + kA\frac{\sigma_2 - \sigma_3}{\sigma_1 - \sigma_3} - \frac{k^2A^2\left(1 + \dfrac{\sigma_1 - \sigma_2}{\sigma_1 - \sigma_3}\right)}{kA\dfrac{\sigma_1 - \sigma_2}{\sigma_1 - \sigma_3} + F}\left(1 + \frac{\sigma_2 - \sigma_3}{\sigma_1 - \sigma_3}\right) \tag{3.10}$$

Assuming $\sigma_1(\varepsilon_1 = \infty, \varepsilon_3 = -\infty) = \text{const.}$, H should be 0,

$$\therefore \quad F = \frac{k\left(1 + \dfrac{\sigma_1 - \sigma_2}{\sigma_1 - \sigma_3}\right)\left(1 + \dfrac{\sigma_2 - \sigma_3}{\sigma_1 - \sigma_3}\right) - \dfrac{\sigma_1 - \sigma_2}{\sigma_1 - \sigma_3}\left(1 + k\dfrac{\sigma_2 - \sigma_3}{\sigma_1 - \sigma_3}\right)}{1 + k\dfrac{\sigma_2 - \sigma_3}{\sigma_1 - \sigma_3}}kA \tag{3.11}$$

$$D = \frac{A - F}{\pi} \tag{3.12}$$

For example, the simulation procedure for stress–strain curves becomes:

(c1) Assign negative ε_3 increment,

(c2) Calculate $A'(\varepsilon)$ by Eq. 3.4,

(c3) Calculate ε_1 by Eq. 3.2,

(c4) Calculate σ_1 by Eq. 3.1,

(c5) Iterate steps (c2−c4) until convergence,

(c6) Calculate ε_2 by Eq. 3.3, and

(c7) Iterate steps (c1−c6) until ε_3 reaches -0.045.

The ordinary triaxial compression data of Kamisunagawa sandstone (Fujii and Ishijima, 1998) is first approximated, then the true triaxial behavior is predicted. The approximation procedure is the same as steps (b1−b5). The results are shown in Figs. 3.1 and 3.2. The experiment is under axial strain control, and the solid simulated curve is under lateral strain control. The simulated stress drop assuming axial strain control (dashed line) can be compared to the experimental results (Fig. 3.1a). The predicted stress–strain curves for σ_2 from 20 to 80 MPa are shown in Fig. 3.1b−d. The stress–strain curves under $\sigma_2 = \sigma_3$ for Kamisunagawa sandstone are approximated well. ε_2 exhibits extensile behavior for low to moderate σ_2 (Fig. 3.1a−c), however, it shows contraction for high σ_2 (Fig. 3.1d). The peak stress–σ_2 relationships (Fig. 3.2) under $\sigma_2 = \sigma_3$ and $\sigma_2 > \sigma_3$ are both linear.

Stress–strain curves under σ_2 = 300 MPa and σ_3 = 100 MPa for Cretaceous–Tertiary boundary (KTB) amphibolite (Fig. 3.3a, Chang and Haimson, 2000), and under σ_2 = 125 MPa and σ_3 = 50 MPa for Coconino sandstone (Fig. 3.3b, Ma and Haimson, 2016) are approximated well by the simple 3D model. This model requires only four parameters (A = 90 GPa, C = 2, ε_s = 0.0035, and k = 0.22 for Fig. 3.3a; A = 37.5 GPa, C = 1.5, ε_s = 0.0025, and k = 0.217 for Fig. 3.3b), although the peak stress–σ_2 relationship is not considered. Stress-dependent k in the next chapter is introduced to approximate the convex peak stress–σ_2 relationship.

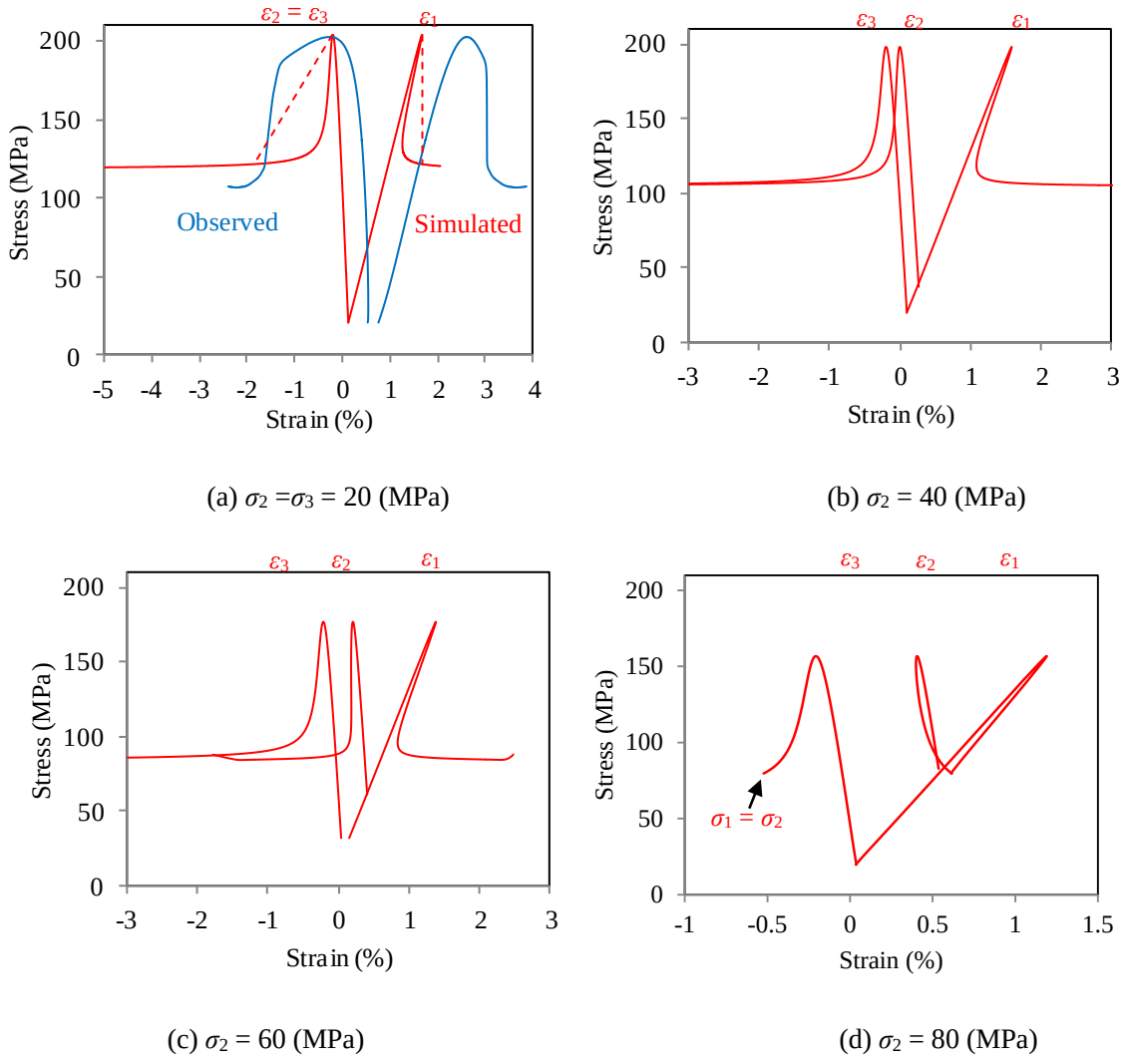

(a) σ_2 =σ_3 = 20 (MPa)

(b) σ_2 = 40 (MPa)

(c) σ_2 = 60 (MPa)

(d) σ_2 = 80 (MPa)

Fig. 3.1 Effects of σ_2 on stress-strain curves by setting A = 13 (GPa), C = 3.25, ε_s = 0.0025 and k = 0.182. The observed stress-strain curves of Kamisunagawa sandstone are under ordinary triaxial compression.

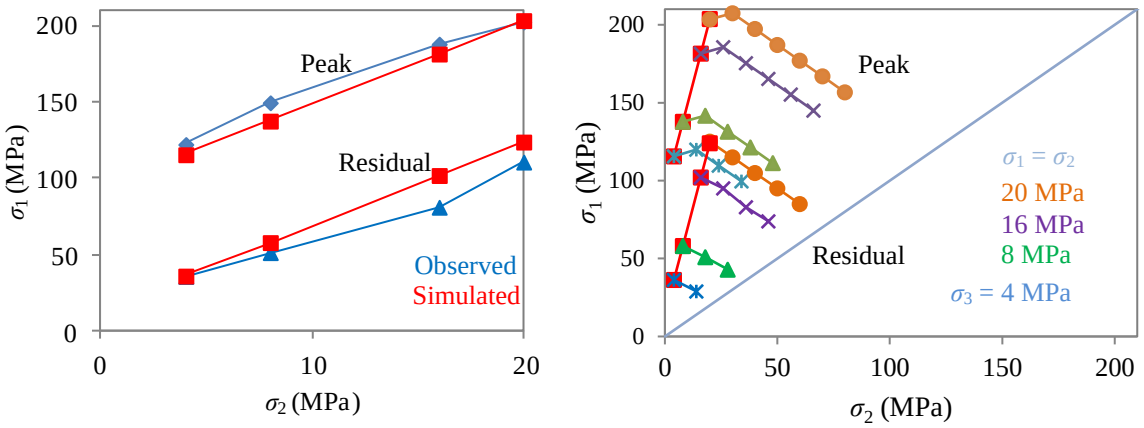

(a) $\sigma_2 = \sigma_3$ (b) $\sigma_2 > \sigma_3$

Fig. 3.2 Peak stress under ordinary triaxial compression and true triaxial compression. The observed failure envelope of Kamisunagawa sandstone is under ordinary triaxial compression.

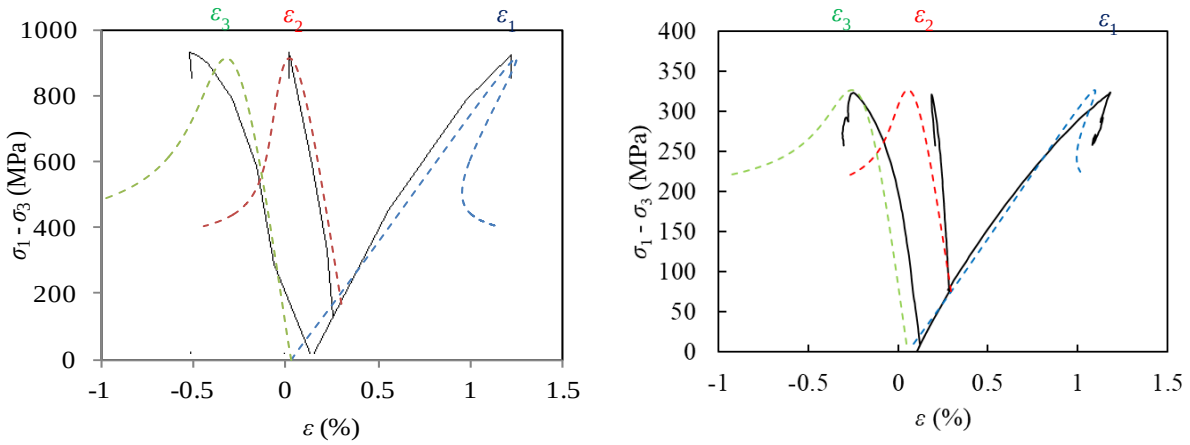

(a) KTB amphibolite (b) Coconino sandstone

Fig. 3.3 Stress-strain curves under (a): σ_2 = 300 (MPa) and σ_3 = 100 (MPa) for KTB amphibolite (Chang and Haimson, 2000) and (b): σ_2 = 125 (MPa) and σ_3 = 50 (MPa) for Coconino sandstone (Ma and Haimson, 2016). The dashed/solid lines are the simulated/experimental results.

4. Modified 3D model

4.1 Introduction of k dependent on confining pressure

The stress-dependent k (Eq. 4.1 and Fig. 4.1) is introduced with an additional term $-\beta\sigma_2$ compared to Eq. 2.1:

$$k = \frac{\Delta k}{\pi}\left[\tan^{-1}\left\{\frac{1}{\alpha}\left(\sigma_3 - \beta\sigma_2 - \sigma_0\right)\right\} + \frac{\pi}{2}\right] + k_0 \tag{4.1}$$

where β is a constant to adjust the effect of σ_2, taking a value between 0 (no effect) and 1 (the same effect as σ_3).

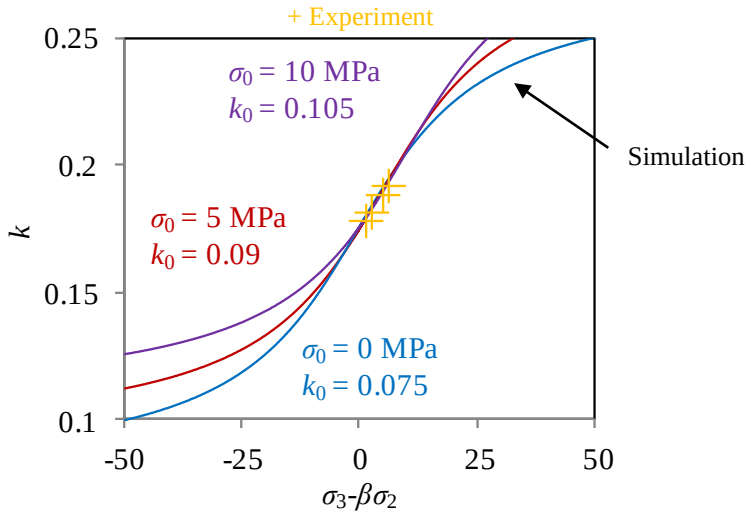

Fig. 4.1 Stress-dependent elastic modulus k by the Δk = 0.2, β = 0.7, k_0 = 0.105, σ_0 = 10, and α = 20 (MPa).

For example, the calculation procedure for stress–strain curves becomes:

(d1) Assign negative ε_3 increment,

(d2) Calculate $A'(\varepsilon)$ by Eq. 3.4,

(d3) Calculate ε_1 by Eq. 3.2,

(d4) Calculate σ_1 by Eq. 3.1,

(d5) Calculate ε_2 by Eq. 3.3,

(d6) Calculate k by Eq. 4.1,

(d7) Iterate steps (d2−d6) until k converges, and

(d8) Iterate steps (d1−d7) for loading until ε_3 reaches -0.045.

4.2 Prediction of the intermediate principal stress effects

The stress–strain curves under $\sigma_2 = \sigma_3$ and $\sigma_2 > \sigma_3$ for Kamisunagawa sandstone is approximated again using this modified 3D model. The approximation procedure is the same as the steps (b1−b7), except that (b7') was executed instead of (b7):

(b7') Use a nonlinear least-squares method for k vs. $\sigma_3 - \beta\sigma_2$ curve to obtain values of k_0, Δk, α, and σ_0 at assigned β.

The results (Fig. 4.2) look similar to those (Fig. 3.1) without stress-dependent k; however, the peak stress for true triaxial compression increases and then decreases with σ_2 (Fig. 4.3b), showing true triaxial behavior. The convexity of the peak stress curves under true triaxial compression can be controlled by parameters k_0 and σ_0 (Figs. 4.4 and 4.5). Therefore, the modified 3D model is expected to approximate the results of true triaxial compression. The experimental results obtained under at least three different values of σ_2 and σ_3 are needed for approximation. Moreover, biaxial compression and extension can also be predicted (Fig. 4.6).

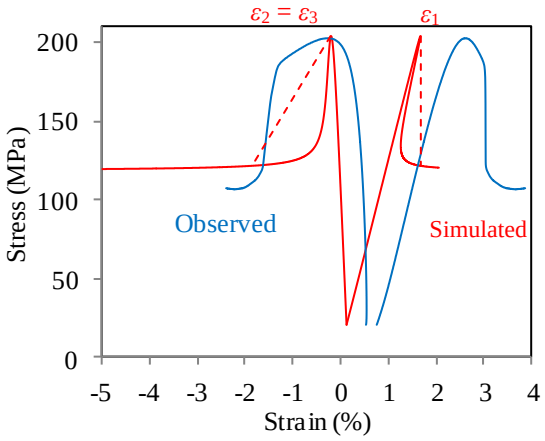

(a) $\sigma_2 = \sigma_3 = 20$ (MPa)

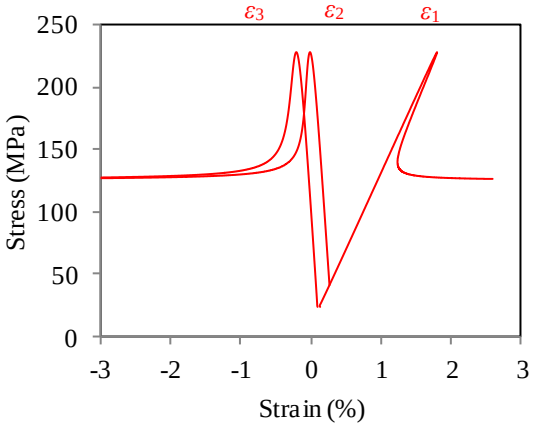

(b) $\sigma_2 = 40$ (MPa)

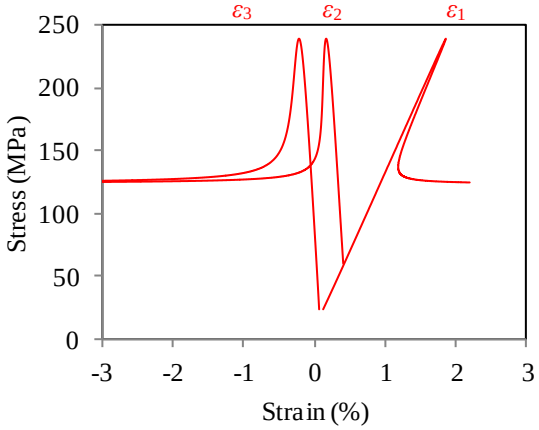

(c) $\sigma_2 = 60$ (MPa)

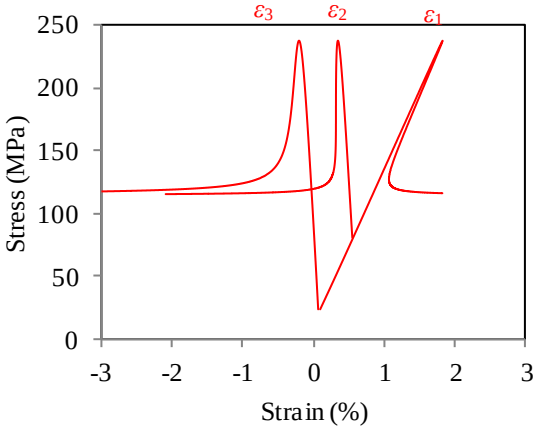

(d) $\sigma_2 = 80$ (MPa)

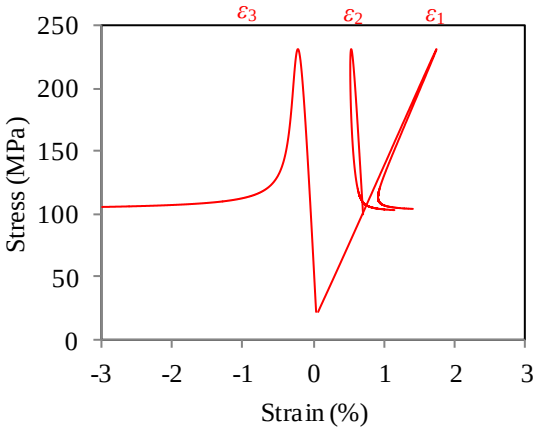

(e) $\sigma_2 = 100$ (MPa)

Fig. 4.2 Effects of intermediate principal stress on stress-strain curves for A = 13 (GPa), C = 3.25, ε_s = 0.0025, Δk = 0.2, β = 0.7, k_0 = 0.105, σ_0 = 10, α = 20 (MPa), and σ_3 = 20 (MPa). The observed stress-strain curves of Kamisunagawa sandstone are under ordinary triaxial compression.

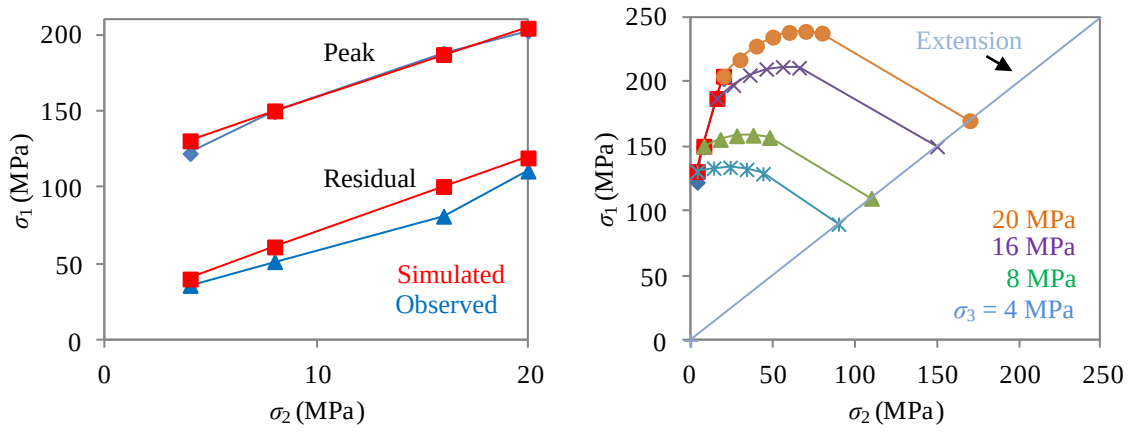

(a) $\sigma_2 = \sigma_3$ (b) $\sigma_2 > \sigma_3$

Fig. 4.3 Peak stress under ordinary triaxial compression and true triaxial compression. The observed failure envelope of Kamisunagawa sandstone is under ordinary triaxial compression.

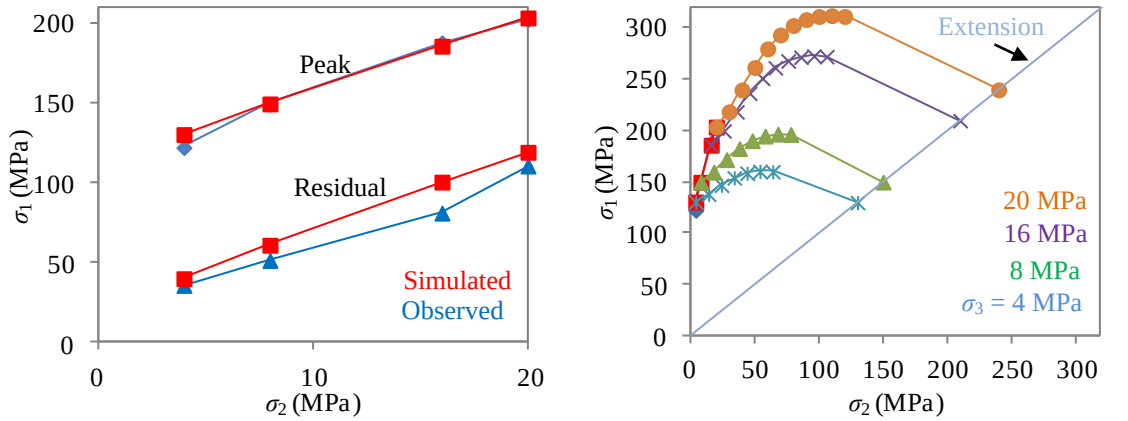

(a) $\sigma_2 = \sigma_3$ (b) $\sigma_2 > \sigma_3$

Fig. 4.4 Peak stress under ordinary triaxial and true triaxial compression by setting $k_0 = 0.075$ and $\sigma_0 = 0$ (MPa). The observed failure envelope of Kamisunagawa sandstone is under ordinary triaxial compression.

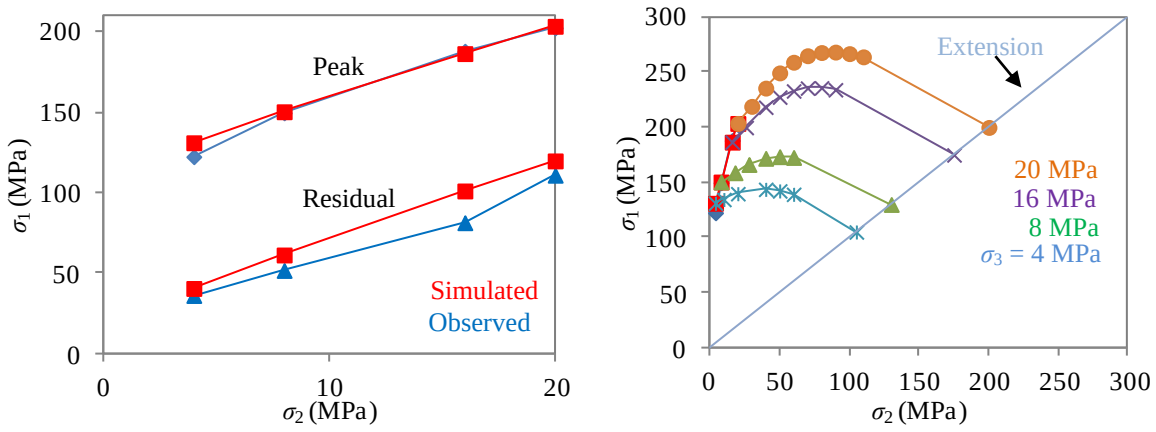

(a) $\sigma_2 = \sigma_3$ (b) $\sigma_2 > \sigma_3$

Fig. 4.5 Peak stress under ordinary triaxial and true triaxial compression by setting $k_0 = 0.09$ and $\sigma_0 = 5$ (MPa). The observed failure envelope of Kamisunagawa sandstone is under ordinary triaxial compression.

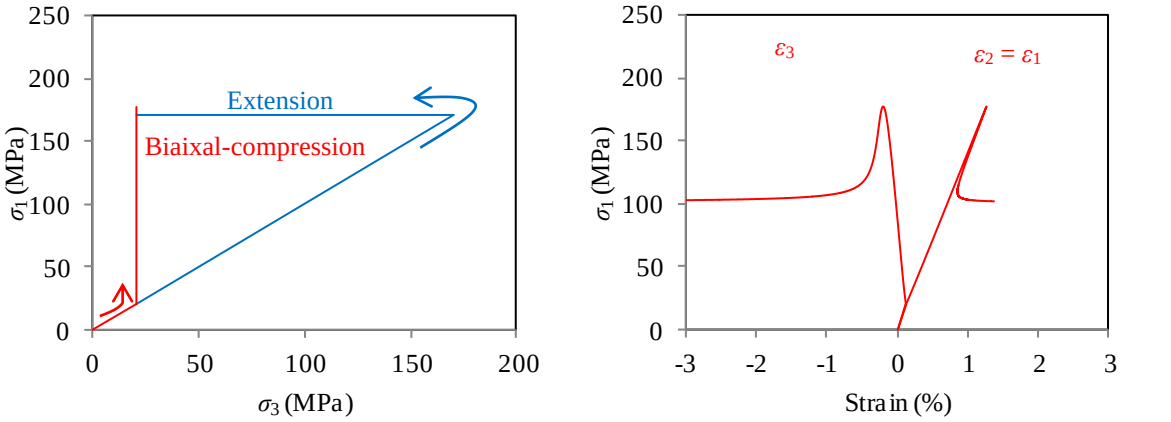

(a) Loading path (b) Biaxial-compression behavior

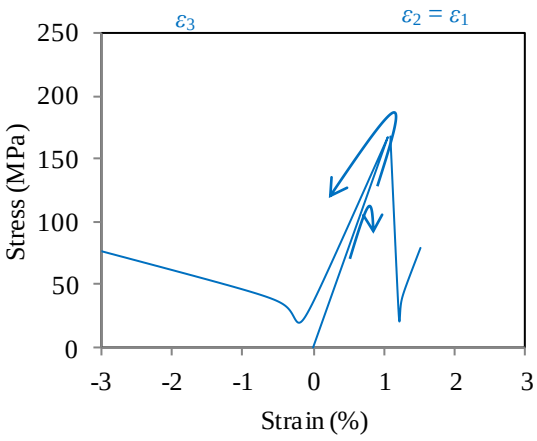

(c) Extension behavior

Fig. 4.6 Biaxial compression and extension behavior obtained under different loading paths.

The modulus A' according to the simulation, is shown in Fig. 4.7. $A'(\varepsilon_1)$ slightly increases with compression. $A'(\varepsilon_3)$ decreases with lateral expansion, with the decrease itself decreasing with σ_2. The A' (ε_2) is reversely evaluated from the results as

$$A'(\varepsilon_2) = \frac{\sigma_2 - kA(\varepsilon_1 + \varepsilon_3)}{\varepsilon_2} \tag{4.2}$$

and it behaves in a very complex manner (Fig. 4.7c). However, this complexity does not make the simulation difficult because $A'(\varepsilon_2)$ is not required to obtain the results and is calculated inversely.

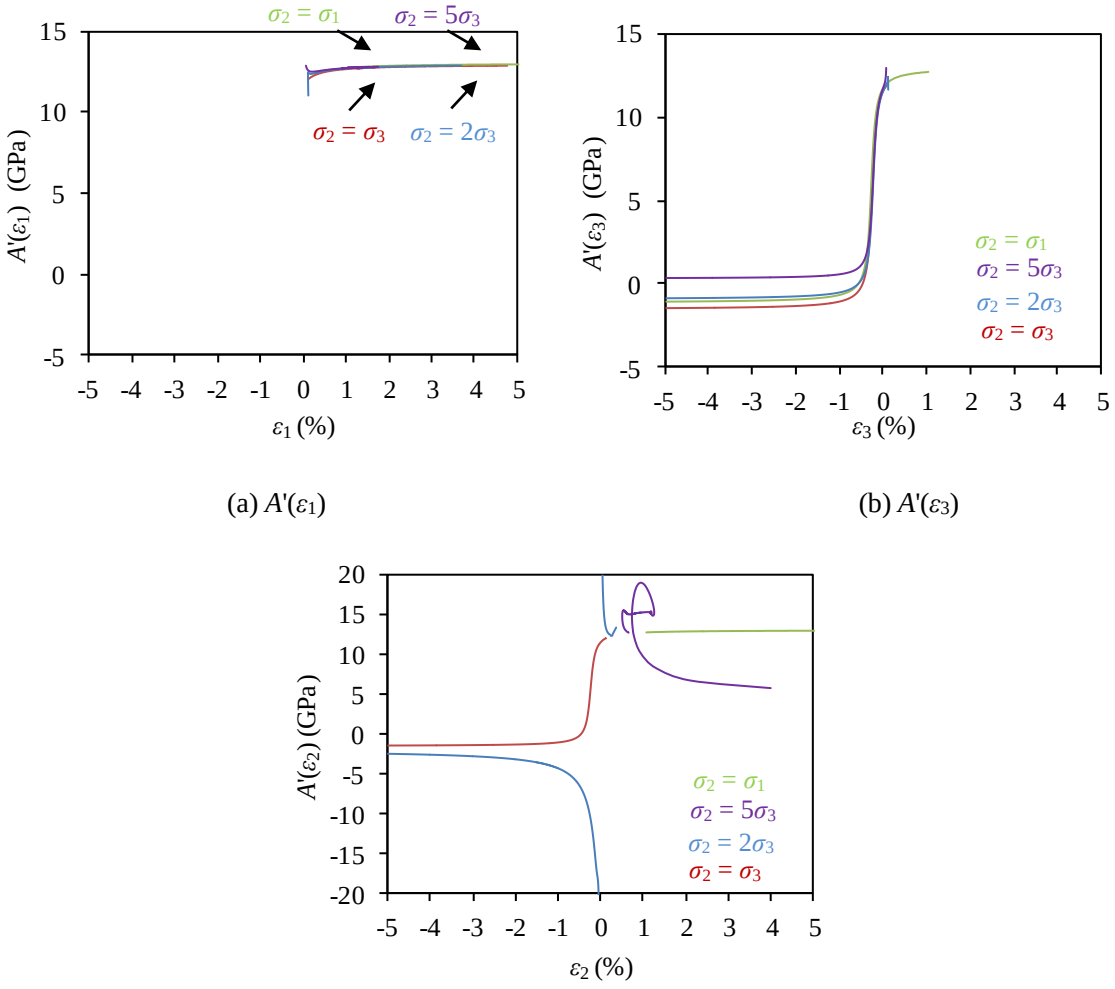

(a) $A'(\varepsilon_1)$ (b) $A'(\varepsilon_3)$

(c) $A'(\varepsilon_2)$

Fig. 4.7 Strain-dependent elastic modulus A'.

4.3 Approximation of true triaxial data

In chapter 3, the true stress–strain curves of KTB amphibolite (Chang and Haimson, 2000) and Coconino sandstone (Ma and Haimson, 2016) were simulated well by the 3D constitutive model for specific values of σ_2 and σ_3. The stress–strain curves and peak stress–σ_2 relationship for Westerly granite (Haimson and Chang, 2000) and the two rocks are above approximated using the modified 3D model. The following steps are added to the approximation steps above (b1−b5):

(e6) Assume β at 0.3, 0.5, 0.7, and 0.9,

(e7) Obtain k vs. σ_3 - $\beta\sigma_2$ curve for $\sigma_2 = \sigma_3$,

(e8) Assume k_0 (e.g., 0.075, 0.080, 0.085, 0.090, and 0.095 for Westerly granite),

(e9) Obtain values of Δk, α, and σ_s by a nonlinear least-squares method (e.g., Fig. 4.8),

(e10) Calculate stress–strain curves and failure envelopes,

(e11) Iterate steps (e8−e10),

(e12) Iterate steps (e6−e11), and

(e13) Select a set of parameters that can best simulate the peak stress–σ_2 curve under $\sigma_2 > \sigma_3$.

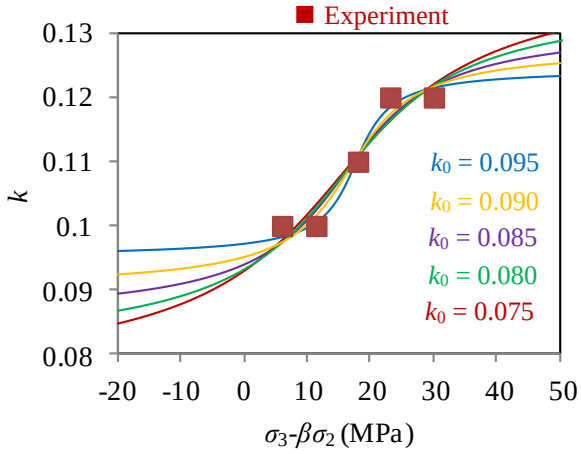

Fig. 4.8 Example of k vs. σ_3 - $\beta\sigma_2$ for Westerly granite (Haimson and Chang, 2000) for A = 58.5 (GPa), C = 2, ε_s = 0.0007 and β = 0.7. The fitting lines were obtained by a nonlinear least-squares method. k_0 = 0.085 gave the best results in the case.

An example plot of k vs. σ_3 - $\beta\sigma_2$ for Westerly granite with β = 0.7 is shown in Fig. 4.8. The parameter values were obtained for each k_0 by a nonlinear least-squares method. The failure envelopes of all rock types for $\sigma_2 = \sigma_3$ (Figs. 4.9a, 4.10a, and 4.11a) were approximated reasonably well. The true stress–strain curves of rock (Figs. 4.9c, 4.10c, and 4.11c) under the modified 3D model were somewhat different from

those under the simple 3D model (Fig. 3.2) because the former prioritized approximating the failure envelope. For Westerly granite and KTB amphibolite, the failure envelope for $\sigma_2 > \sigma_3$ at high σ_3 was simulated well, while the modified 3D model underestimates the peak stress at low σ_3 (Figs. 4.9b and 4.10b). For sandstone, this model simulated the failure envelope well for $\sigma_2 > \sigma_3$ at low σ_3, while it overestimates the peak stress at high σ_3 (Fig. 4.11b).

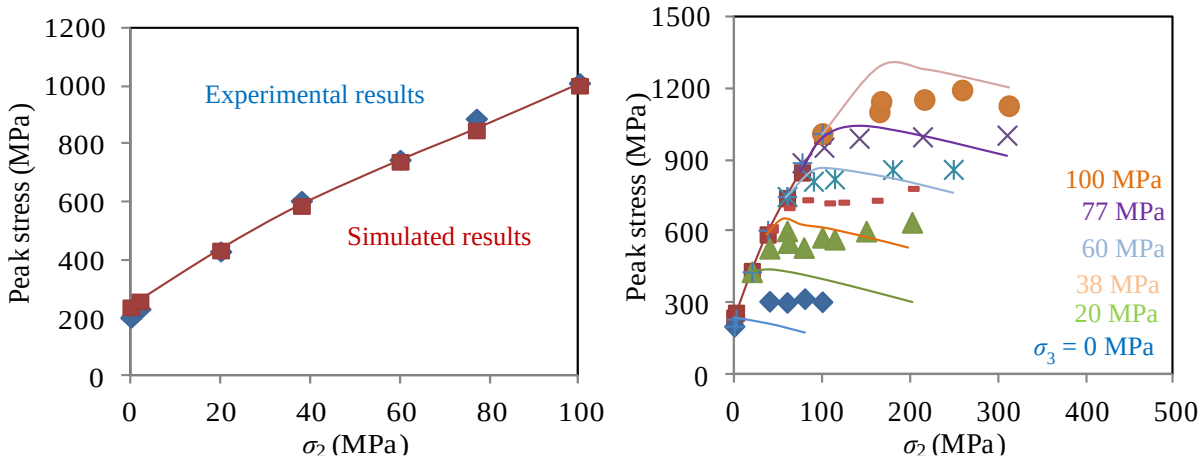

(a) Failure envelope for $\sigma_2 = \sigma_3$ (b) Failure envelope for $\sigma_2 > \sigma_3$

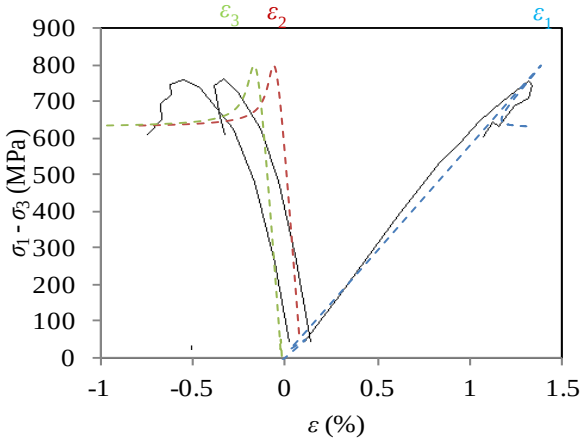

(c) Example of true stress strain curves for $\sigma_2 = 114$ (MPa) and $\sigma_3 = 60$ (MPa)

Fig. 4.9 Approximation by the modified 3-D model for Westerly granite by parameters A = 58.5 (GPa), C = 2, ε_s = 0.0007, α = 11.05 (MPa), σ_0 = 16.01 MPa, Δk = 0.0467, and k_0 = 0.085. (a): Failure envelope for $\sigma_2 = \sigma_3$. (b): Failure envelope for $\sigma_2 > \sigma_3$. The lines/symbols were simulated/experimental results by 3-D equations/ Haimson and Chang, 2000. (c): Example of true stress strain curves for σ_2 = 114 (MPa) and σ_3 = 60 (MPa). The dashed/solid lines are the simulated/experimental results.

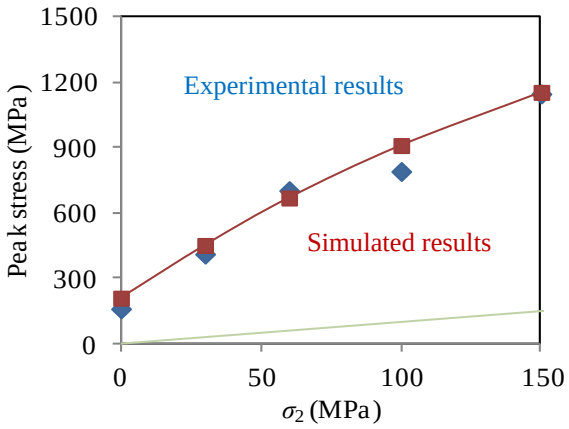

(a) Failure envelope for $\sigma_2 = \sigma_3$

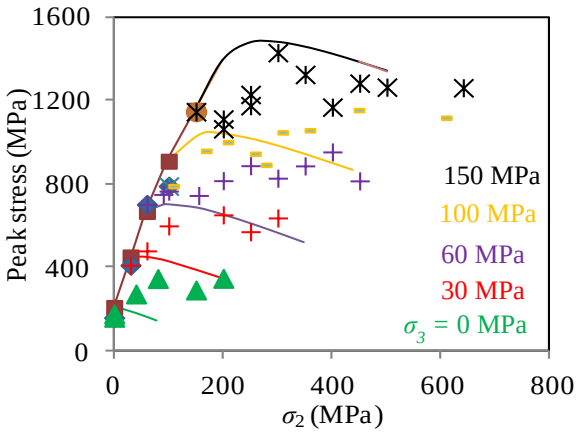

(b) Failure envelope for $\sigma_2 > \sigma_3$

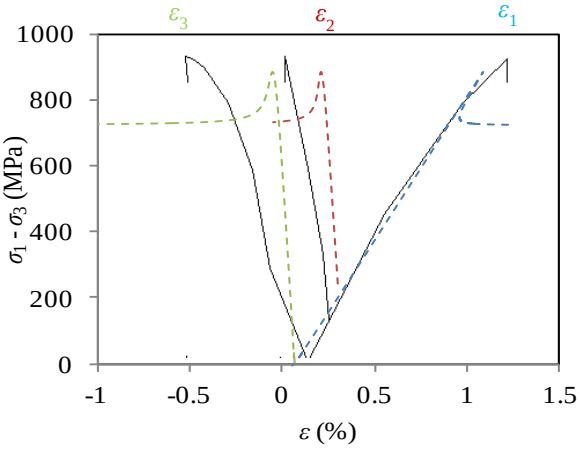

(c) Example of true stress strain curves for σ_2 = 300 (MPa) and σ_3 = 100 (MPa)

Fig. 4.10 Approximation by the modified 3D model for KTB amphibolite by parameters A = 90 (GPa), C = 2, ε_s = 0.0005, α = 24.8 (MPa), σ_0 = 33.2 MPa, Δk = 0.0792, and k_0 = 0.1. (a): Failure envelope for $\sigma_2 = \sigma_3$. (b): Failure envelope for $\sigma_2 > \sigma_3$. The lines/ symbols were calculated/experimental results by 3D equations/Chang and Haimson, 2000. (c): Example of true stress strain curves for σ_2 = 300 (MPa) and σ_3 = 100 (MPa). The dashed/solid lines are the simulated/experimental results.

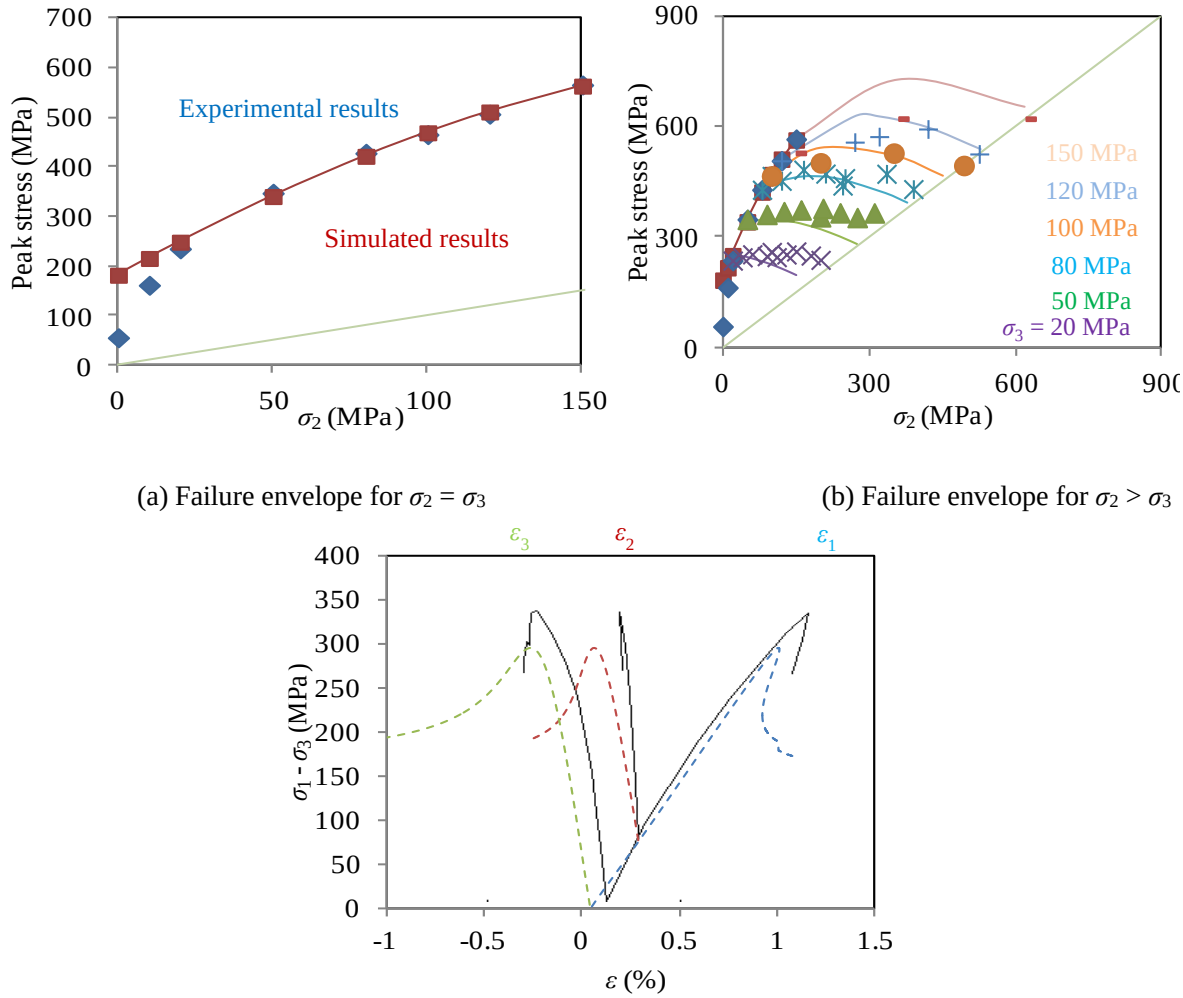

(a) Failure envelope for $\sigma_2 = \sigma_3$

(b) Failure envelope for $\sigma_2 > \sigma_3$

(c) Example of true stress strain curves for σ_2 = 125 (MPa) and σ_3 = 50 (MPa)

Fig. 4.11 Approximation by the modified 3D model for sandstone by parameters A = 37.5 (GPa), C = 1.5, ε_s = 0.0025, α = 54.5 (MPa), σ_0 = 86.0 MPa, Δk = 0.702, and k_0 = 0.14. (a): Failure envelope for $\sigma_2 = \sigma_3$. (b): Failure envelope for $\sigma_2 > \sigma_3$. The lines/ symbols were calculated/experimental results by 3D equations/Ma and Haimson, 2016. (c): Example of true stress strain curves for σ_2 = 125 (MPa) and σ_3 = 50 (MPa). The dashed/solid lines are the simulated/experimental results.

4.4 Comparison with other 3D criteria

3D failure criteria are compared in Fig. 4.12a (Priest, 2005, Zhang and Zhu, 2007, Lee et al., 2012, Jiang and Zhao, 2015, and Li et al., 2021) from Li et al. (2021).

Simplified Priest criterion (Priest, 2005):

$$\sigma_1 = 3[w\sigma_2 + (1-w)\sigma_3] + \sigma_c[m_b \frac{w\sigma_2 + (1-w)\sigma_3}{\sigma_c}]^a - (\sigma_3 + \sigma_2) \tag{4.3}$$

$$m_b = \exp\left(\frac{GSI - 100}{28 - 14D}\right) m_i \tag{4.4}$$

$$w \approx \alpha\sigma_3^{\beta} \tag{4.5}$$

Zhang-Zhu criterion (Zhang and Zhu, 2007):

$$s\sigma_c = \frac{9}{2\sigma_c}\tau_{oct}^2 + \frac{3}{2\sqrt{2}} m_i \tau_{oct} - m_i \frac{(\sigma_1 + \sigma_3)}{2} \tag{4.6}$$

$$s = \exp\left(\frac{GSI - 100}{9 - 3D}\right) \tag{4.7}$$

$$\tau_{oct} = \frac{1}{3}\left[(\sigma_1 - \sigma_2)^2 + (\sigma_2 - \sigma_2)^2 + (\sigma_3 - \sigma_1)^2\right]^{1/2} \tag{4.8}$$

Jiang-Zhao criterion (Jiang and Zhao, 2015):

$$\frac{1}{m_b \sigma_c^{1/a-1}} (\sqrt{3J_2})^{1/a} + \frac{2\cos(\pi/3 - \theta)}{\sqrt{3}} \sqrt{J_2} - \frac{s\sigma_c}{m_b} - \frac{I_1}{3} = 0 \tag{4.9}$$

$$J_2 = \frac{1}{6}\left[(\sigma_1 - \sigma_2)^2 + (\sigma_2 - \sigma_2)^2 + (\sigma_3 - \sigma_1)^2\right] \tag{4.10}$$

$$I_1 = \sigma_1 + \sigma_2 + \sigma_3 \tag{4.11}$$

Lee criterion (Lee et al., 2012):

$$\sqrt{2J_2} - g_{ww}(\theta, I_1) = 0 \tag{4.12}$$

$$J_2 = \frac{1}{6}\left[(\sigma_1 - \sigma_2)^2 + (\sigma_2 - \sigma_2)^2 + (\sigma_3 - \sigma_1)^2\right] \tag{4.13}$$

$$I_1 = \sigma_1 + \sigma_2 + \sigma_3 \tag{4.14}$$

The peak stress–σ_2 relationship is also plotted in Fig. 4.12a by the modified 3D model. Some of these criteria give better results than the proposed model but do not give a reasonable nonlinear stress–strain relationship. Therefore, using one of these criteria is better when the stress–strain relationship is almost linear, and the failure envelope must be followed strictly. However, using my proposed model to represent

nonlinear stress–strain relationships well while following the true triaxial failure envelope is better.

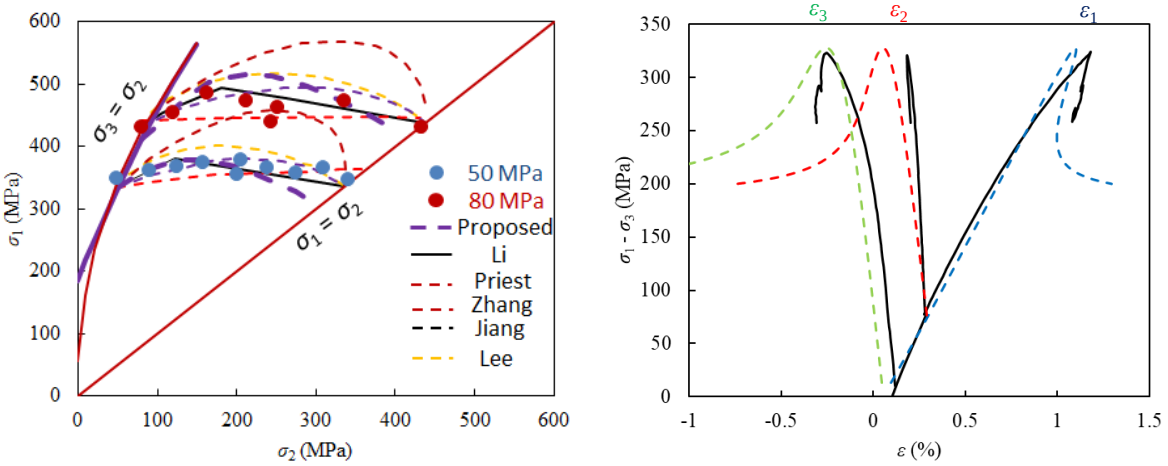

(a) (b)

Fig. 4.12 (a) Approximated results by modified 3D model with A = 37.5 GPa, C = 1.5, ε_s = 0.0025, α = 48 MPa, σ_0 = 20 MPa, Δk = 0.3, and k_0 = 0.15. Other approximated results by 3D failure criteria (Priest, 2005, Zhang and Zhu, 2007, Lee et al., 2012, Jiang and Zhao, 2015, and Li et al., 2021) from Li et al. (2021). (b) Example of true stress-strain curves by modified 3D model. The dashed/solid lines are the simulated/experimental results.

4.5 Axial unloading behaviors

The equations for the proposed models give the same axial stress–strain curves while unloading as during loading; this is unrealistic. Therefore, beyond the equations, the axial unloading behavior should be defined. Because microcracks hardly grow during axial unloading, an assumption is proposed, i.e., that strains decrease elastically with decreasing stress according to the elastic moduli at the beginning of axial unloading:

$$\Delta\sigma_1 = A(\varepsilon_{1u})\Delta\varepsilon_1 + k(\sigma_{1u},\sigma_{2u},\sigma_{3u})A(\varepsilon_{2u})\Delta\varepsilon_2 + k(\sigma_{1u},\sigma_{2u},\sigma_{3u})A(\varepsilon_{3u})\Delta\varepsilon_3 \quad (4.15)$$

$$\Delta\sigma_2 = k(\sigma_{1u},\sigma_{2u},\sigma_{3u})A(\varepsilon_{1u})\Delta\varepsilon_1 + A(\varepsilon_{2u})\Delta\varepsilon_2 + k(\sigma_{1u},\sigma_{2u},\sigma_{3u})A(\varepsilon_{3u})\Delta\varepsilon_3 \quad (4.16)$$

$$\Delta\sigma_3 = k(\sigma_{1u},\sigma_{2u},\sigma_{3u})A(\varepsilon_{1u})\Delta\varepsilon_1 + k(\sigma_{1u},\sigma_{2u},\sigma_{3u})A(\varepsilon_{2u})\Delta\varepsilon_2 + A(\varepsilon_{3u})\Delta\varepsilon_3 \quad (4.17)$$

where $\Delta\sigma$ and $\Delta\varepsilon$ are the changes in stress and strain, respectively, and σ_u and ε_u are the stress and strain,

respectively, at the beginning of axial unloading. This model gives reasonable axial unloading curves (Fig. 4.13).

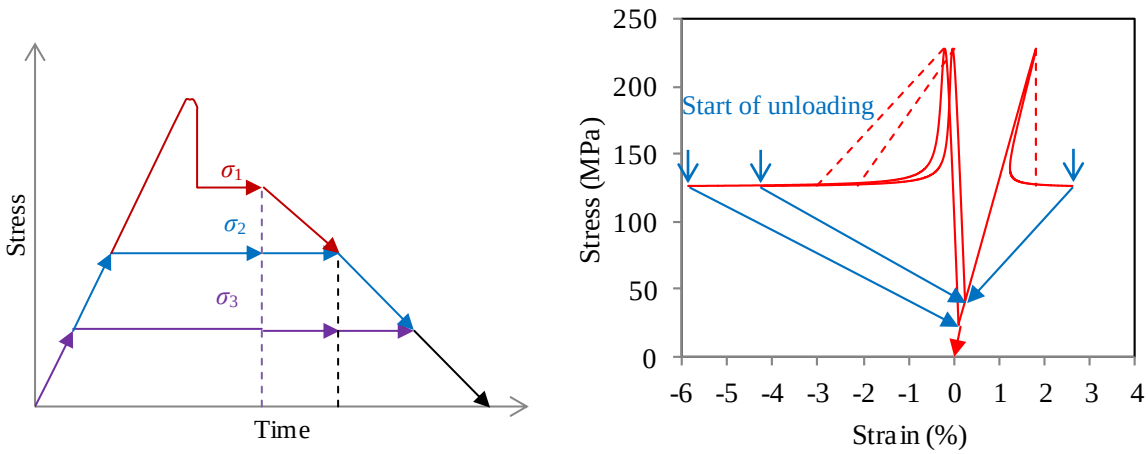

(a) Loading pattern (b) Example of unloading behavior for σ_2 = 40 (MPa), and σ_3 = 20 (MPa)

Fig. 4.13 Unloading behavior (values of parameters are the same as Fig. 4.2).

4.6 Discussions

To represent the stress-strain curves and failure envelopes for rocks, the simple 2D model needs at least two tests under one uniaxial and one triaxial, and the modified 2D model needs at least three tests under one uniaxial and two triaxial (Table 4.1). Also, the simple 3D model needs at least two tests under one uniaxial and one triaxial, and the modified 3D model needs at least five tests under one uniaxial, two triaxial, one biaxial and one true triaxial (Table 4.2).

Table 4.1 Minimum needed experiments for simple/modified 2D model

Constitutive models	**Solved problems**	**Parameters**	**Minimum needed experiments**
Simple 2D model	Usual 2D	4	1 uniaxial + 1 triaxial
Modified 2D model	2D with convex failure envelope	7	1 uniaxial + 2 triaxial

Table 4.2 Minimum needed experiments for simple/modified 3D model

Constitutive models	**Solved problems**	**Parameters**	**Minimum needed experiments**
Simple 3D model	Usual 3D	4	1 uniaxial + 1 triaxial
Modified 3D model	3D with convex failure envelope	8	1 uniaxial + 2 triaxial + 1 biaxial + 1 true triaxial

5. Conclusions

In order to propose a 3D constitutive model for rocks that can represent realistic true triaxial stress-strain curves and convex failure envelopes with fewer parameters, the simple 2D model previously proposed by our research group was first modified to have a convex failure criterion. The effects of the parameters on the failure envelope were observed, and a procedure to approximate the stress-strain curves and failure envelopes was proposed. This model approximated these much better than conventional 2D models. The model was applied to a pressurized thick-walled cylinder under the plane strain condition.

The simple 2D constitutive model was then extended to a simple 3D model, which was used to simulate the ordinary triaxial compression data of a rock and predict its true triaxial behavior. True triaxial stress-strain curves under specific values of σ_2 and σ_3 were approximated reasonably. However, the predicted peak stress–σ_2 relationship was linear.

Finally, the 3D model was developed by introducing stress-dependent k. The peak stress–σ_2 relationship for true triaxial compression first increased and then decreased with σ_2 as actual rocks. The constitutive equations can also simulate biaxial compression and axial extension behaviors with the same parameters. True triaxial stress-strain curves and failure envelopes were simulated reasonably. A method to represent axial unloading behavior was also proposed.

This modified 3D model is the only one that can fairly represent the true triaxial nonlinear stress-strain curves and convex failure envelopes. Refining and introducing the 3D model to 3D FEM may make numerical stress analysis of rock structures more realistic. In particular, for the problems in which σ_2 effects (Fig. 5.1) are significant such as rockburst (Yun et al., 2010).

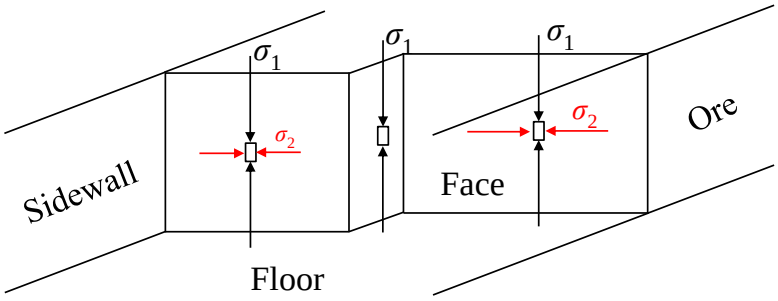

Fig. 5.1 Stress states at the boundary of a mine opening.

References

Al-Ajmi AM, Zimmerman RW (2005), Relation between the Mogi and the Coulomb failure criteria, Int. J. Rock Mech. Min. Sci., 42 (3), pp. 431-439.

Bruning, T., Karakus, M., Nguyen, G.D. and Goodchild, D. (2018), Experimental study on the damage evolution of brittle rock under triaxial confinement with full circumferential strain control, Rock Mech. Rock Eng. 51(11): 3321–3341.

Chang, C. and Haimson, B. (2000), True triaxial strength and deformability of the German Continental deep drilling program (KTB) deep hole amphibolites, J. Geophys. Res., 105, pp. 18999-19013.

Cecilio, D.L., Devloo, P.R.B., Gomes, S.M., dos Santos, E.R.S., and Shauer, N., (2015), An improved numerical integration algorithm for elastoplastic constitutive equations. Comp. Geotech., 64, pp. 1-9.

Cho, N. Martin, C.D. and Sego, D.C. (2007), A clumped particle model for rock, International Journal of Rock Mechanics and Mining Sciences, 44, pp. 997-1010.

Crouch, S. L. and Fairhurst, C. (1973), Mechanics of coal mine bumps and the interaction between coal pillars mine roof and floor. U. S. B. M. Contract Report, H0101778.

Cristescu, N. (1987), Elastic viscoplastic constitutive equations for rock. Int. J. Rock Mech. Min. Sci. & Geomech. Abstr., Vol. 24, No., pp. 271-282.

Cristescu, N. and Hunsch, U. (1991), Determination of nonassociated constitutive equation for rock salt from experiments. IUTAM Symposium Hannover/Germany 1991, pp. 511-523.

Ewy, R. (1999), Wellbore-stability predictions by use of a modified Lade criterion, SPE Drill Completion, 14 (2), pp. 85-91.

Feng, X. T., Haimson, B., Li, X. C., Chang, C. D., Ma, X. D., Zhang, X. W., Ingraham, M., and Suzuki, K (2019), ISRM Suggested Method: determining deformation and failure characteristics of rocks subjected to true triaxial compression, Rock Mech. Rock Eng., 52 (6), pp. 2011-2020

Fujii, Y. and Ishijima, Y. (1998a), Simple constitutive equations for Brittle Rocks, based on strain-dependent stiffness, Advances in Rock Mechanics, Eds. by Lin, Y. et al., World Scientific Publishing, Singapore, New Jersey, London, Hong Kong, pp. 186-193.

Fujii, Y. and Ishijima, Y. (1998b in Japanese), Constitutive equations for rock, Based in Radial Stiffness Decrease, Shigen-to-Sozai Vol, 114 p. 169-174.

Fujii, Y., Kiyama, T., Ishijima, Y. and Kodama, J. (1998), Examination of a rock failure criterion based on

circumferential tensile strain, Pure and Applied Geophysics, Vol. 152, No. 3, pp. 551-577.

Frantziskonis, G. and Desai, C.S. (1987), Constitutive model with strain softening, Int. J. Solids Struct., 23 (6), pp. 733-750.

Jiang, H., Wang, X. W. and Xie, Y. L. (2011), New strength criteria for rocks under polyaxial compression. Can. Geotech. J., 48(8):1233–1245.

Jiang, H. and Zhao, J. (2015), A simple three-dimensional failure criterion for rocks based on the Hoek-Brown criterion, Rock Mech. Rock Eng., 48, pp. 1807-1819.

Haimson, B. C. and Chang, C. (2000), A new true triaxial cell for testing mechanical properties of rocks, and its use to determine strength and deformability of Westerly granite, Int. J. Rock Mech. Min. Sci., 37, pp. 285-297.

Hallbauer, D. K., Wagner, H. and Cook, N. G. W. (1973), Some observations concerning the microscopic and mechanical behavior of Quartzite specimens in stiff, Triaxial Compression Tests, Int. J. Rock Mech. Min. Sci. & Geomech. Abstr., 10, pp. 713-726.

Hoek, E. and Brown, E.T. (1980), Empirical strength criterion for rock masses, J. Geotech. Geoenviron. Eng., 106 (GT9), pp. 1013-1035.

Hoek, E., Carranza-Torres, C. and, Corkum, B. (2002), Hoek-Brown failure criterion - 2002 edition, Proceeding of 5th North American Rock Mechanics Symposium and Tunneling Association of Canada Conference, pp. 267-273, Toronto.

Ismael, M. and Konietzky, H., (2019). Constitutive model for inherent anisotropic rocks: ubiquitous joint model based on the Hoek-Brown failure criterion, Comput. Geotech., 105, pp. 99-109.

Goodman, R. E. (1980), Introduction to Rock Mechanics, John Wiley and Sons.

Lade, P., and Duncan J. (1975), Elastoplastic stress–strain theory for cohesionless soil, J. Geotech. Eng. ASCE, 101 (10), pp. 1037-1053.

Lajtai, E. Z. (1998), Microscopic fracture process in a granite, Rock Mech. Rock Eng., 31, pp. 237-250.

Li, C., Prikryl, R., Nordlund, E. (1998), The stress-strain behaviour of rock material related to fracture under compression, Eng. Geol., 49 (3–4), pp. 293-302.

Li, H., Guo T., Nan Y. and Han B. (2021), A simplified three-dimensional extension of Hoek-Brown strength criterion, Journal of Rock Mechanics and Geotechnical Engineering, 44(1): 1365-1609.

Lee Y. K., Pietruszczak S., and Choi B. H. (2012), Failure criteria for rocks based on smooth

approximations to Mohr–Coulomb and Hoek–Brown failure functions, Int. J. Rock Mech. Min. Sci., 56, pp. 146-160.

Ma, X. and Haimson, B. (2016), Failure characteristics of two porous sandstones subjected to true triaxial stresses, Journal of Geophysical Research-Solid Earth, 121 pp. 6477-6498.

Martin, C. D. and Chandler, N. A. (1993), Stress heterogeneity and geological structures, International Journal of Rock Mechanics and Mining Sciences & Geomechanics Abstracts, Volume 30, Issue 7, Pages 993-999.

Melkoumian, N., Priest, S. and Hunt, S. P. (2009), Further development of the three-dimensional Hoek–Brown yield criterion, Rock Mech. Rock Eng., 42(6):835–847.

Mogi, K. (1967), Effect of the intermediate principal stress on rock failure, Journal of Geophysical Research, 72 (20), pp. 5117-5131.

Mogi, K. (1971a), Effect of the triaxial stress system on the failure of dolomite and limestone, Tectonophysics, 11, pp. 111-127.

Mogi, K. (1971b), Fracture of rocks under high triaxial compression, Journal of Geophysical Research, 76 (5), pp. 1255-1269.

Mogi, K. (2007), Experimental rock mechanics, Taylor and Francis, London.

Nishitani, H. (1994), Computational and experimental fracture mechanics, Computational Mechanics Publications, Berlin.

Okubo, S. and Fukui, K. (2006), An analytical investigation of a variable-compliance-type constitutive equation, Rock Mechanics and Rock Engineering, Vol. 39, No. 3. pp. 233–253.

Pan, X. D. and Hudson, J. A. (1988), A simplified three dimensional Hoek–Brown yield criterion. In: Romana M (ed) Rock mechanics and power plants. Balkema, Rotterdam, pp 95–103.

Pourhosseini, O. and Shabanimashcool, M. (2014), Development of an elasto-plastic constitutive model for intact rocks, Int. J Rock Mech. Min. Sci., 66, pp. 1-12.

Priest, S. (2005), Determination of shear strength and three-dimensional yield strength for the Hoek–Brown criterion. Rock Mech. Rock Eng., 38(6):299–327.

Senent S., Jimenez R., Reyes A. (2013), Numerical simulation of the influence of small-scale defects on the true-triaxial strength of rock samples. Comput. Geotech. 53:142–156.

Singh, M. and Singh, B. (2008), High lateral strain ratio in jointed rock masses, Eng. Geol. 98:75–85.

Wang, S., Xu, W., Wang, W., Jia, C. (2018), Experimental and numerical investigations on the mechanical behavior of fine-grained sandstone, Int. J. Geomech., 18 (2), Article 04017150.

Wawersik, W. R. and Fairhurst, C. 1970, A study of brittle rock fracture in laboratory compression experiments, International Journal of Rock Mechanics and Mining Sciences & Geomechanics Abstracts, Volume 7, Issue 5, Pages 561-575.

Weng, M. C., Jeng F. S., Hsieh T. M. and Huang T. H. (2008), A simple model for stress-induced anisotropic softening of weak sandstones, International Journal of Rock Mechanics and Mining Sciences, 45, pp. 155-166.

Xie, N., Zhu, Q. Z., Xu, L. H., and Shao, J. F. (2011), A micromechanics-based elastoplastic damage model for quasi-brittle rocks, Comput. Geotech., 38, pp. 970-977.

Yang, S. Q., Jing, H. W., and Wang, S. Y. (2012), Experimental investigation on the strength, deformability, failure behavior and acoustic emission locations of red sandstone under triaxial compression, Rock Mech. Rock. Eng., 45 (4), pp. 583-606.

You, M. (2009), True-triaxial strength criteria for rock, Int. J. Rock Mech. Min. Sci., 46: 115-127.

Yun, X., Mitri, Hani S., Yang, X., and Wang, Y. (2010), Experimental investigation into biaxial compressive strength of granite, International Journal of Rock Mechanics and Mining Sciences, Volume 47, Issue 2, Pages 334-341, ISSN 1365-1609, https://doi.org/10.1016/j.ijrmms.2009.11.004.

Zhang, J. C. (2018), Experimental and modelling investigations of the coupled elasto-plastic damage of a quasi-brittle rock. Rock Mech. Rock Eng., 51, pp. 465-478.

Zhang, K., Zhou, H., and Shao, J. F. (2013), An experimental investigation and an elastoplastic constitutive model for a porous rock, Rock Mech. Rock Eng., 46, pp. 1499-1511.

Zhang, L. (2008), A generalized three-dimensional Hoek–Brown strength criterion. Rock Mech. Rock Eng., 41(4):893–915.

Zhang, L. and Zhu, H. (2007), Three-dimensional Hoek–Brown strength criterion for rocks. J. Geotech. Geoenviron. Eng., 133(9):1128–1135.

Zhao, X. G. and Cai, M. (2010), A mobilised dilation angle model for rocks, International Journal of Rock Mechanics and Mining Sciences, 47, pp. 368-384.